A THERMODYNAMIC AUDIT OF THE SURFACE ENERGY BUDGET OF THE HUDSON BAY COMPLEX (HBC) FROM 1980 – 2024 USING THE ECMWF ERA5 CLIMATE REANALYSIS MODEL

HALEY B KLASSEN

A THESIS SUBMITTED TO

THE FACULTY OF GRADUATE STUDIES

IN PARTIAL FULFILLMENT OF THE REQUIREMENTS

FOR THE DEGREE OF

MASTER OF SCIENCE

GRADUATE PROGRAM IN GEOGRAPHY

YORK UNIVERSITY

TORONTO, ON

NOVEMBER 2025

Abstract

This study presents a thermodynamic audit of the HBC for 1980–2024 using ECMWF ERA5 reanalysis to quantify long-term changes in the surface energy budget. Basin-wide warming is evident, with increases in net shortwave (K*) and incoming longwave (L↓) radiation, despite no significant trend in incoming solar radiation (K↓). These changes are linked to declining surface albedo and enhanced greenhouse forcing, increasing regional energy retention. Subsurface heat fluxes (Qs) show spatial redistribution, with warming advancing northward from JB into central HB and HS. The ice-covered season has shortened while the open-water period has lengthened by weeks and mean annual sea-ice cover has declined by 2–4% per decade.

The resulting energy imbalance marks a transition from an ice-dominated to a thermodynamically active open-water regime, affecting ocean–atmosphere coupling, primary productivity, and ecosystem stability. Surface temperature (T_0) warming and increased L↓ likely drive shifting sea-ice seasons, underscoring HBC's climate sensitivity.

Acknowledgements

I would like to express my deepest gratitude to my supervisors, Dr. Bello and Dr. Higuchi, for their invaluable guidance, insight, and support throughout this research. Their expertise, thoughtful feedback, encouragement, and enthusiasm have been instrumental in shaping the direction and quality of this work. I am truly grateful for their mentorship and for the opportunity to learn under their supervision in the Geography Graduate Program within the Faculty of Environmental and Urban Change at York University. I also wish to extend my sincere appreciation to my colleagues and peers within the faculty. Their shared commitment to research and academic excellence created a supportive and inspiring environment that greatly enriched my experience. I would also like to extend my appreciation and thanks to Dr. Tarmo Remmel for his help with the coding used to extract and condense the data to a useable format, which made the data so much easier to interpret and use.

I am profoundly grateful to my family for their unwavering patience, encouragement, and belief in me. Your continuous support has been the foundation of my perseverance and success. To my friends, thank you for your understanding, optimism, and companionship during this process. Your encouragement and kindness have provided balance and motivation through every stage of this journey. Finally, I would like to acknowledge all those who, in various ways, have contributed to the completion of this work. Your support and inspiration have been deeply appreciated.

Table of Contents

List of Figures

List of Tables

List of Symbols

Symbol	Description	Units
Q^*	Net Radiation	$MJ/m^2/y$
Q_H	Sensible Heat Flux	$MJ/m^2/y$
Q_E	Latent Heat Flux	$MJ/m^2/y$
Q_S	Subsurface Heat Flux	$MJ/m^2/y$
K_{ex}	Shortwave Radiation TOA	$MJ/m^2/y$
K^*	Net Shortwave Radiation	$MJ/m^2/y$
$K\downarrow$	Incoming Shortwave Radiation	$MJ/m^2/y$
L^*	Net Longwave Radiation	$MJ/m^2/y$
$L\downarrow$	Incoming Longwave Radiation	$MJ/m^2/y$
Q_P	Precipitation Energy Flux	$MJ/m^2/y$
Q_{SH}	Sensible Heat Flux from Precipitation	$MJ/m^2/y$
Q_{Lf}	Latent Heat Flux from Melting Snow	$MJ/m^2/y$
P	Precipitation	mm
E	Evaporation	mm
α	Albedo	%
L_f	Latent Heat of Fusion	0.334 MJ/kg
c_{water}	Specific Heat of Pure Water	0.004184 MJ/kg*°C
c_{ice}	Specific Heat of Ice	0.00209 MJ/kg*°C
C_{sw}	Specific Heat of Sea Water	0.00399 MJ/kg*^{0}C
T_0	Surface Temperature	°C
T_{2m}	Air Temperature 2m above sea level	°C
ε	Surface Emissivity	0.97 unitless
σ	Stefan-Boltzmann Constant	$5.67*10^{-8}$ $Wm^{-1}K^{-4}$

Chapter 1 – Introduction

1.1 Introduction

The Hudson Bay Complex (HBC)—encompassing Hudson Bay, James Bay, Foxe Basin and Hudson Strait—represents one of the most seasonally ice-covered regions in the Northern Hemisphere. As a marginal sea located at the southern edge of the Arctic, the HBC is sensitive to atmospheric variability and climate forcing mechanisms. Over the past several decades, substantial changes in sea ice cover have been observed, characterized by delayed freeze-up, earlier breakup, and overall reductions in ice extent and thickness (Hochheim & Barber, 2014; Tivy et al., 2011). These transformations are of critical concern due to the HBC's ecological importance, ice-albedo feedbacks are critical in global climate regulation, and HBC is essential in this process, and its cultural significance to Indigenous communities who rely on the ice for transportation, hunting, and cultural continuity (Gearheard et al., 2010).

Atmospheric forcings, such as warming surface air temperatures, altered wind fields, and large-scale climate oscillations, have been identified as primary drivers of sea ice variability in the HBC. Climate phenomena like the Arctic Oscillation (AO) and North Atlantic Oscillation (NAO) exert strong influence on atmospheric circulation patterns, which in turn affect sea ice drift, thermodynamic growth, and melt processes (Bello & Higuchi, 2019; Deser et al., 2000). Furthermore, the recent amplification of Arctic warming due to anthropogenic greenhouse gas emissions has intensified the impact of these forcings, making the sea ice regime more dynamic and less predictable (Stroeve et al., 2012). While much of the existing research has focused on pan-Arctic trends, regional studies are essential to understanding the nuanced responses of specific basins like the HBC to atmospheric drivers.

Despite the importance of the Hudson Bay Complex in Arctic and sub-Arctic climate systems, it remains relatively underrepresented in global cryosphere studies. The region's unique geographic and oceanographic characteristics—such as shallow bathymetry, freshwater inflow from major rivers, and limited connectivity to the central Arctic Ocean—create a distinct sea ice environment that may respond differently to external forcings compared to other Arctic regions (Saucier et al., 2004). Understanding these region-specific dynamics is critical for improving climate model projections and for supporting local adaptation strategies.

This thesis investigates the impacts of atmospheric forcings and thermodynamics on sea ice variability and long-term trends in the HBC. By integrating observational datasets, satellite remote sensing products, and reanalysis climate data, the study will (1) characterize recent changes in sea ice phenology and extent; (2) evaluate the influence of key atmospheric drivers, including surface temperature anomalies; and (3) assess spatial and temporal heterogeneity in sea ice response across the sub-basins of the HBC. Through this approach, the research will contribute to a more comprehensive understanding of how atmospheric conditions are reshaping sea ice dynamics in one of the most climatically responsive regions of the Arctic.

1.2 Objectives

The purpose of this study is to utilize the data obtained from the 5th generation of the global atmospheric reanalysis (ERA5) model to understand the behaviour and observed changes in sea ice coverage across HBC over the past 45 years. Specific objectives of the study are:

a) Perform a thermodynamic audit of the HBC over the 45-year study period.
b) Determine which, if any, thermodynamic factors are driving any observed changes.
c) Summarize the impact each factor is having on the HBC,
d) Postulate future impacts and suggest further areas of research.

Chapter 2 – Literature Review

2.1 Seasonal Patterns of Sea-Ice in the Hudson Bay Complex (HBC)

The HBC undergoes a complete annual freeze-thaw cycle, making it a critical region for studying seasonal sea-ice dynamics. This literature review synthesizes current research on the seasonal patterns of sea ice in the HBC, highlighting recent trends, atmospheric influences, and ecological implications (Andrews et al., 2018). Historically, the HBC experiences sea-ice formation from north to south between September and December, with melting occurring generally from south to north between May and August. The region is predominantly covered by first-year ice, which varies in thickness due to local atmospheric and oceanic conditions (Andrews et al., 2018).

Recent observations indicate significant changes in the HBC's sea-ice patterns. In spring 2024, southeastern Hudson Bay experienced record early sea-ice loss, with median opening dates occurring up to 49 days earlier than the 1979–2023 median. This anomaly was driven by above-average temperatures and unusual wind patterns (Soriot et al., 2025). Climate models tend to overestimate the ice-free period in the HBC by about 30 days. This bias is primarily due to regional atmospheric temperature inaccuracies and misrepresentations of wind patterns (Crawford et al., 2023). Variability in wind patterns significantly affects sea-ice thickness and distribution. For instance, stronger northwesterly winds have been linked to increased ice thickness in eastern Hudson Bay, delaying spring break-up by several weeks (Kirillov et al., 2020).

The changing sea-ice dynamics have profound effects on the HBC's ecosystem (Crawford et al., 2023). The polar bear population in Hudson Bay has declined by approximately 50% over the past four decades. The reduction in sea ice limits their hunting grounds, leading to prolonged fasting periods and increased mortality (Dickie & Dickie, 2024). Alterations in sea-ice patterns disrupt the entire marine food web, affecting species from algae to beluga whales. The extended ice-free periods and warmer waters can lead to habitat loss and changes in species distribution (Soriot et al., 2025).

Studies utilizing historical records, such as Hudson's Bay Company ship logs, have reconstructed sea-ice conditions dating back to the 18^{th} century. These records provide valuable insights into long-term sea-ice variability and trends in the HBC (Andrews et al., 2018). Overall, the bay is experiencing significant shifts in its seasonal sea-ice patterns, driven by climatic changes. These alterations have cascading effects on the region's ecology, particularly concerning species reliant on sea ice. Continued monitoring and improved modeling are essential for understanding and mitigating the impacts of these changes (Kirillov et al., 2020).

2.2 Recent Trends in Sea-Ice Extent (SIE)

Hudson Bay, located in northeastern Canada, is a seasonally ice-covered inland sea that undergoes a complete freeze-thaw cycle annually. The extent of sea ice in Hudson Bay is a key metric for assessing environmental change, with significant implications for regional ecosystems, Indigenous communities, and global climate models. Over recent decades, satellite observations and historical records have documented noticeable reductions in sea-ice extent and changes in its seasonal timing. Traditionally, sea ice begins forming in Hudson Bay in late October to early November, reaching maximum extent by March, and breaking up from late May through July. The entire Bay typically becomes ice-covered during winter, with coverage approaching 100% in most years (Gough et al., 2004).

Historical analyses using Canadian Ice Service charts and ship log data reveal that prior to the mid-20th century, ice cover was more extensive and persisted longer into the spring (Catchpole & Halpin, 1987). Since 1980, passive microwave satellite data has allowed for more accurate quantification of extent, showing an overall declining trend in both total coverage and seasonal duration (Tivy et al., 2011). Recent research confirms a clear decline in average sea-ice extent in Hudson Bay; Between 1980 and 2010, the maximum winter extent has remained stable (since most of the Bay still freezes), but the onset of freeze-up has delayed by 2–3 weeks, and breakup has advanced by up to 4 weeks (Hochheim & Barber, 2014). The total duration of sea-ice cover has decreased by approximately 7–9 weeks in the last four decades, and interannual variability is high and is influenced by large-scale atmospheric patterns such as the Arctic Oscillation and North Atlantic Oscillation (Gough et al., 2004). Notably, southeastern Hudson Bay, including the area around the Belcher Islands, has exhibited the earliest and most rapid reductions in sea-ice extent, attributed to regional oceanic warming and wind-driven export of ice (Soriot et al., 2025).

Climate models, project continued reductions in sea-ice extent throughout the 21st century. However, these models tend to overestimate ice-free conditions due to biases in representing surface air temperatures and local wind effects (Crawford et al., 2023). Even under moderate CO_2 emissions, summer ice extent is expected to decline significantly, with fewer complete freeze-over events in future winters.

Changes in sea-ice extent have cascading ecological and social impacts. Reduced ice coverage limits hunting grounds for polar bears and affects migration and foraging patterns of marine mammals such as beluga whales and seals. Declines in ice cover disrupt nutrient cycling and primary productivity, which are tightly coupled with ice presence and melting patterns (Barbedo et al., 2020; Steiner et al., 2015). Indigenous communities reliant on ice for travel and subsistence activities face growing safety risks and cultural disruption. Hudson Bay's sea-ice extent has shown a significant downward trend, particularly in the timing of freeze-up and breakup. While the bay still undergoes complete seasonal coverage, the period of open water is increasing (Bello & Higuchi, 2019). Climate models suggest this trend will continue, potentially altering Hudson Bay’s physical and biological systems profoundly. Ongoing monitoring, incorporation of Indigenous knowledge, and refinement of regional models are essential for accurate forecasting and adaptation.

2.3 Underlying Processes of Change

Recent decades have witnessed significant alterations in its sea ice dynamics, influenced by both natural variability and anthropogenic climate change. Understanding the underlying processes driving these changes is crucial for predicting ecological impacts and informing management strategies. Atmospheric conditions play a pivotal role in shaping sea ice distribution and thickness within the HBC. Kirillov (2020) identified a pronounced west-east asymmetry in sea ice thickness, attributing this pattern to cyclonic atmospheric circulation. Specifically, north-northwesterly winds during the winter season in 2016/2017 led to thicker ice in southern Hudson Bay, while enhanced west-northwesterly winds in 2017/2018 resulted in thicker ice in eastern Hudson Bay, delaying spring break up by approximately 30 days. This study underscores the importance of atmospheric forcing in determining regional ice thickness patterns and their implications for seasonal ice dynamics.

Additionally, studies have highlighted the influence of wind patterns on sea ice dynamics. Wang et al. (1994) demonstrated that strengthened northerly winds are associated with heavy ice conditions, while Saucier and Dionne (1998) showed that increased river runoff can lead to thicker ice in southeast Hudson Bay due to freshening of the mixed layer. These findings emphasize the complex interplay between atmospheric and oceanic processes in shaping sea ice characteristics. The seasonal cycle of sea ice in the HBC is experiencing shifts, with earlier ice retreat and delayed formation. Crawford et al. (2024) analyzed Coupled Model Intercomparison Project Phase 6 (CMIP6) models and found that 73% overestimate the ice-free period, primarily due to regional atmospheric temperature biases and inaccuracies in wind patterns. These biases have significant implications for predicting future sea ice conditions and understanding ecological impacts.

The alterations in sea ice dynamics have profound effects on the HBC's ecosystem. Polar bears, for instance, rely on sea ice for hunting seals. The extension of the ice-free period from approximately 120 days to 150 days over the past three decades has increased fasting durations, negatively impacting survival and reproductive success. Similarly, earlier ice breakup disrupts the timing of under-ice phytoplankton blooms, which are essential for the marine food web. The sea ice dynamics of the Hudson Bay Complex are influenced by a complex interplay of atmospheric forcing, seasonal ice phenology, and ecological interactions (Bello & Higuchi, 2019). While natural variability contributes to these changes, anthropogenic climate change is accelerating the processes, leading to earlier ice retreat and extended ice-free periods. Addressing the biases in climate models and understanding the regional dynamics are crucial for accurate predictions and effective management of the HBC ecosystem.

2.4 Sea-Ice Thermodynamics

The thermodynamic evolution of sea ice in Hudson Bay is governed by a complex interplay of atmospheric, oceanic, and radiative energy exchanges. As a seasonally ice-covered inland sea with a shallow bathymetry and strong freshwater influence, Hudson Bay presents a unique setting for the study of sea ice thermodynamics. Its annual cycle, characterized by rapid freeze-up in late fall and extensive melt during early summer, is modulated by specific energetic components that interact nonlinearly across temporal and spatial scales.

The surface energy balance is postulated to be one of the primary drivers of thermodynamic processes in Hudson Bay, along with the heat budget. Net shortwave radiation (K*) plays a dominant role in ice melt during spring and early summer, especially due to the pronounced ice-albedo feedback. As ice and snow surfaces thin or fragment, surface albedo (α) drops from typical winter values of ~0.85 to as low as 0.40, significantly increasing K* absorption (Hochheim & Barber, 2010). Incoming longwave radiation ($L_{\downarrow}$), particularly during overcast and humid conditions, modulates both melt and freeze processes by altering net radiative loss from the surface ($L^* = L_{\downarrow} - L_{\uparrow}$), especially during shoulder seasons. During winter, surface heat loss is dominated by net longwave radiation and turbulent fluxes—sensible (Q_H) and latent heat fluxes (Q_E)—which together contribute to the conductive cooling necessary for ice growth (Bello & Higuchi, 2019). Air–ice temperature gradients and wind speed influence these turbulent fluxes significantly, with higher wind speeds enhancing Q_H and Q_E during cold air outbreaks.

Recent studies highlight the amplification of thermodynamic changes due to feedback mechanisms. The ice–albedo feedback is especially strong in Hudson Bay, where sea ice loss in spring increases solar absorption, enhancing melt onset and accelerating the timing of breakup (Tivy et al., 2011). Reflected solar radiation shows uneven decline across the study area, leading to increases in net radiation driven by the decreases in albedo during the summer season (Bello & Higuchi, 2019). Furthermore, warming atmospheric trends over the past three decades have led to earlier onset of melt (by up to 3 weeks) and delayed freeze-up (by 1–2 weeks), reducing the duration of the ice season (Derksen et al., 2012; Hochheim & Barber, 2014). These changes are also reflected in the shifting energy partitioning in the surface budget—greater partitioning into K^* and $L_\downarrow$, with reduced net heat loss during autumn. Numerical sea ice models, attempt to resolve the complex thermodynamics of Hudson Bay ice. However, accurately capturing processes such as snow–ice formation, melt pond evolution, and the impacts of variable snow cover remains a challenge.

2.5 Research Gaps and Limitations

Studies have revealed that HBC's ice seasons have changed. Late freeze-up has been added to earlier break-up and a longer ice-free season. Though the ice-covered season is sometimes disregarded, studies primarily look at break-up and freeze-up dates, from which the ice-free season is estimated. Although sea-ice season dates have been extensively researched, little is understood about the physical mechanisms impacting the ice-albedo feedback. This demonstrates the significance of time-series observations in comprehending the underlying thermodynamic processes and the seasonal evolution of sea ice cover. In HBC, declining SIE is a known truth. It is generally accepted that atmospheric temperature rises due to rising GHG concentrations are the primary cause of sea-ice variations. According to Bello & Higuchi (2019), sea-ice loss and increased radiation gains, rather than air temperature increases, are the main causes of the current warming that has occurred throughout HBC over the past 20 years. Many studies in the past have not looked at how the HBC system can be further affected by stronger positive albedo feedback. This demonstrates how crucial energetics are to the HBC system. The significance of comprehending the ice-seasons was further underscored by the changes in albedo and energetics; variations in the energetic in each ice season are unknown in terms of duration and length.

The most significant unanswered question is the extent to which heat losses from open-water versus ice-covered areas of HBC account for the difference in sea ice retreat and decline. To date, models and current energetic investigations across the HBC have paid little to no consideration to this important research subject. To comprehend the causes driving change, coupled models (dynamic + thermodynamic) are employed using a similar methodology to Munir's (2020) paper on the same subject. Even in studies that use coupled models, most of the research tends to concentrate primarily on dynamic forces in the redistribution of ice, even though it is well established that energy excess during extended ice-free and early break-up has contributed to late freeze-up.

However, in reaction to energy fluxes at the top and bottom of the water column, ice grows and decays vertically. Ice undergoes a vertical diffusion process that modifies internal temperature as a result of heat storage and penetrating sunlight. Sea ice cover can be affected by dynamic processes that cause ice to move, and form leads. Thus, thermodynamic processes play a major role in controlling the development and disintegration of ice; dynamic forces are responsible for subsequent changes in sea ice.

This emphasizes how crucial it is to comprehend the fundamental dynamics that have led to the loss in sea ice throughout HBC over the past 45 years. Finally, in order to comprehend the seasonal variations in ice, time-series observations are essential. These serve as the main topics of the ensuing chapters.

Chapter 3 – Research Design and Methods

3.1 Study Area

The Hudson Bay Complex (HBC) is a vast inland sea located in northeastern Canada, bordered by the provinces of Manitoba, Ontario, and Quebec, and the territory of Nunavut. It is one of the largest bodies of saltwater in the world, covering approximately 1.23 Mkm^2 (Macdonald & Kuzyk, 2011). The Bay connects to the Atlantic Ocean through Hudson Strait and has limited connectivity with the Arctic Ocean via the Foxe Basin and Fury through Hecla Strait. HBC spans roughly 1,370 km (12 degrees of latitude) from north to south and about 1,050 km east to west. It has an average depth of approximately 100 m, reaching a maximum depth of 166 m in HS and a minimum depth of 32 m in JB (DFO, 2010). In comparison to the world's shallowest ocean, the Arctic Ocean, which averages approximately 1000 m deep, the Hudson Bay Complex is very shallow. The region's surrounding terrain is part of the Canadian Shield to the north and east, which is geologically stable and by the Hudson Bay Lowland to the west and south which comprises a vast peatland underlain by gently sloping Ordovician and Silurian dolomites. These regions comprise continuous and discontinuous permafrost.

The Bay receives discharge from a vast drainage basin, nearly 3.9 Mkm^2 making it one of the largest catchment areas in the world. Major river systems feeding into the bay include the Nelson, Churchill, La Grande, and Moose rivers (Déry et al., 2011). Substantial freshwater inputs create a brackish upper layer in the water column, influencing stratification, circulation, and biological productivity. HBC is characterized by a seasonal sea ice regime, with ice formation beginning in late autumn and generally persisting into early summer. Complete ice cover is typically observed by December which starts breaking up in

June, although this timing has shown increasing variability in recent decades (Hochheim & Barber, 2014).

The region's climate is classified as sub-Arctic to low Arctic, with long, cold winters and short, cool summers. Mean annual air temperatures typically range from -5°C to -10°C, and winter temperatures often fall below -30°C (Gough et al., 2004). Precipitation is relatively low, with most falling as snow, and the Bay is influenced by large-scale atmospheric circulation patterns, including the Arctic Oscillation and the North Atlantic Oscillation, which impact seasonal and interannual variability in temperature, sea ice extent, and hydrological fluxes (DFO, 2010). HBC represents a critical component of Canada's northern marine system, functioning as a sensitive indicator of climate variability and change. The Bay's semi-enclosed nature with a dominant counterclockwise flowing current gyre, strong freshwater influence, and extensive seasonal ice cover make it particularly responsive to environmental drivers. As such, it serves as an ideal site for investigating long-term trends in climate variables using reanalysis datasets such as ERA5, with implications for regional ecosystems, carbon cycling, and the livelihoods of Indigenous communities (Macdonald & Kuzyk, 2011).

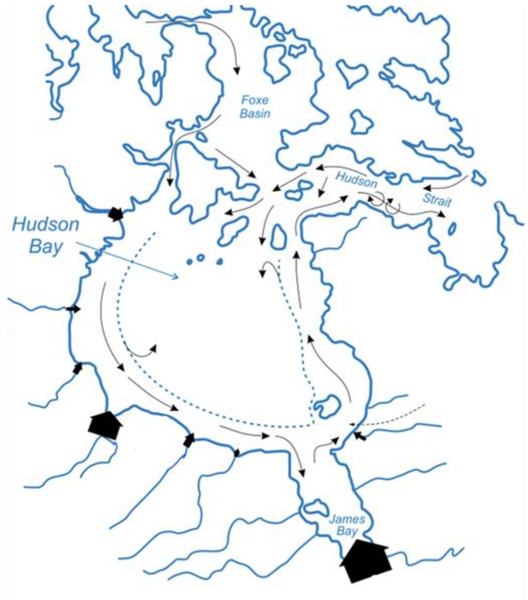

Figure 1 - Visual representation of water circulation pattern plus incoming and outgoing water pathways of the HBC. Source: Kuzyk (2014).

3.2 Model Selection

ERA5 is widely used in model initialization, downscaling, and bias correction. Its compatibility with tools like xarray, netCDF4, and QGIS allows for flexible analysis workflows. ERA5 data is highly suitable for long-term climate data analysis due to several key features that make it both dependable and comprehensive for studying trends, variability, and changes in the Earth's climate system.

ERA5 is the fifth-generation global atmospheric reanalysis produced by the European Centre for Medium-Range Weather Forecasts (ECMWF) as part of the Copernicus Climate Change Service. It replaces the earlier ERA-Interim product and is based on a consistent numerical weather prediction and data assimilation system that extends from 1940 to the present. Like other reanalyses models, ERA5 combines vast amounts of historical weather observations from satellites, ground stations, radiosondes, aircraft, and other sources with a modern numerical model to produce spatially complete and temporally consistent estimates of the atmosphere. These data are available globally at hourly resolution on a 0.25° by 0.25° latitude–longitude grid, with 137 vertical levels reaching the lower mesosphere. Alongside its detailed atmospheric fields, ERA5 also provides estimates of uncertainty, which is especially important in data-sparse regions. Although ERA5 is often described simply as an atmospheric reanalysis, it is in fact a partially coupled system. The model links the atmosphere with the land surface and with an ocean-wave model, so that features such as surface roughness caused by waves can influence the lower atmosphere. However, ERA5 prescribes sea surface temperatures and sea ice concentrations from external observationally based datasets rather than generating them dynamically. This design means that ERA5 can capture two-way feedback between the atmosphere and ocean or sea ice, such as the role of evolving ocean temperatures in driving atmospheric circulation anomalies. Similarly, land surface variables like soil moisture and snow are assimilated separately and then introduced into the atmospheric system, resulting in a coupling between land and atmosphere. ERA5 therefore offers excellent resolution and consistency in its atmospheric and land-surface products, and the two-way coupling model allows it to provide a dynamically evolving picture of the full Earth system.

To address the limitations of this approach, ECMWF has also developed coupled Earth-system reanalyses in which the ocean, atmosphere, and sea ice evolve together, and observations are assimilated simultaneously into multiple components. Examples include the CERA-20C reanalysis, which covers the twentieth century using a coupled atmosphere–ocean framework, and the CERA-SAT reanalysis, which demonstrates the feasibility of coupled reanalysis in the satellite era. These products are better able to represent climate processes that depend on ocean–atmosphere feedback, such as the El Niño–Southern Oscillation and decadal variability. While ERA5 remains the most widely used reanalysis because of its high resolution and accessibility, these coupled reanalyses provide a more physically complete perspective on the Earth system and point toward the direction of future developments in climate reanalysis. Finally, to make ERA5 more directly useful for researchers who require daily rather than hourly data, a derived product has been created that aggregates single-level ERA5 fields into daily statistics. This dataset provides users with daily means, minima, maxima, or sums of variables, sampled at different intervals depending on the needs of the analysis. Because the aggregation is performed dynamically during data retrieval, researchers can tailor the output to their specific requirements without needing to process the large hourly archives themselves. This makes ERA5 not only one of the most advanced atmospheric reanalyses available but also one of the most adaptable, serving a wide range of applications from climate monitoring to hydrology and ecological studies.

ERA5 is freely available through the Copernicus Climate Data Store (CDS) and is continuously updated with a 2- to 3-month latency. This ensures that both historical and near-real-time data can be used in consistent long-term assessments. Numerous studies have validated ERA5 data against observations and other reanalysis products, showing improved accuracy over predecessors like ERA-Interim, especially in areas such as precipitation and hydrological variables (Tarek et al., 2020); surface temperature and wind; and sea level pressure and radiative fluxes. These attributes support accurate trend detection, variability assessment, and attribution studies across global to regional scales.

3.3 Data Collection

ERA5 climate reanalysis data was obtained from the Copernicus Climate Data Store (CDS), maintained by the European Centre for Medium-Range Weather Forecasts (ECMWF). Data was extracted directly from the CDS web interface (*Climate Data Store*, 2025). To access the platform, users must create a free account and log in. Once logged in, datasets can be searched and filtered through the search bar or by browsing the “Climate Data” sections.

For this study, the “ERA5 Daily Aggregated Data on Single Levels from 1950 to Present” dataset was used. The dataset contains pre-processed hourly data aggregated over daily or monthly periods, which reduces post-processing requirements. In the dataset selection page, the following parameters were specified:

- **Variables**: Relevant meteorological variables were selected, the ones selected are listed in Table 1 below along with their units.

Table 1 - ERA5 Variables used for this study, their acronyms used throughout the paper and their respective units. Units used throughout the paper may be converted.

Source: https://cds.climate.copernicus.eu/datasets/derived-era5-single-levels-daily-statistics?tab=download

Variable	**Symbol/Acronym**	**Unit(s)**
Surface Latent Heat Flux	Q_E	J/m^2
Surface Sensible Heat Flux	Q_H	
Surface Net Solar Radiation	K*	
Surface Solar Radiation Downwards	K↓	
Surface Net Thermal Radiation	L*	
Surface Thermal Radiation Downwards	L↓	
Sea-Ice Cover	SIC	Percentage
Snowfall	Snow	m (SWE)
Snow Evaporation	Snow Evap	
Precipitation	Precipitation	
2m Temperature	2m Temp, T_2	Kelvin
Skin Temperature	Skin Temp, T_0	

- **Product Type**: Daily averaged reanalysis
- **Time Period**: January 1st, 1980, to December 31st, 2024.
- **Time**: UTC-05:00
- **Frequency:** 1-hourly
- **Geographical Area**: A bounding box was defined by entering the coordinates for:
    - North 71, South 51, West -95, East -64.
- **Format**: NetCDF (.nc) was selected for ease of use with common climate data analysis tools and R Programming.

Depending on the size of the request, data preparation by the CDS server took anywhere from several minutes to several hours. Once ready, the data file was available for download via a secure download link on the same page or in the user's request history.

Downloaded NetCDF files were processed using climate data software such as:

- Panoply (for quick visualization)
- QGIS (for spatial analysis)
- R's ncdf4 package (for statistical analysis)

Data were reprojected, converted (e.g., Kelvin to Celsius; Joules to megajoules), and partitioned regionally as needed. All datasets were visually inspected to verify completeness, correct temporal coverage, and the physical plausibility of values. Cross-validation with known climate records was used to ensure data integrity. In grid locations containing complex shoreline or islands, the ERA5 sea-ice cover variable N/A flag was used to determine inclusion in this analysis which is solely representative of the marine environment.

3.4 Data Extraction

The extracted data were converted from the .nc file formats into .csv and then .xls Excel files for analysis. The data were extracted using an R-code to convert into a readable format and to reorganize the data to maintain consistency for every spreadsheet, reorganization was to ensure the days of the year (DOY) were listed along the top row (1) and the coordinate points were listed along the first and second columns (A&B). The extracted data was uploaded into QGIS for two reasons: 1) to filter out any data points that have land within the cell and 2) to determine which cell(s) belong to each of the four waterbodies (WB) of interest in this study, Foxe Basin (FB), Hudson Bay (HB), Hudson Strait (HS), or James Bay (JB). Subdividing the HBC into distinct water bodies helps provide a basis for reconciling their distinctive thermal behaviour as FB, HB and JB are aligned along a large latitudinal gradient although their boundaries are defined by somewhat arbitrary divisions (Figure 2). Additionally, Hudson Strait functions as an energy corridor for the entire HBC with the Labrador Sea as well as a distinct regional waterbody.

An aggregated locations spreadsheet titled "AGLOCATIONSHORT" was created which included the new, correctly aggregated locations and their assigned WB was used in another R-code to further filter the 45-years' worth of spreadsheets down from its original study area of 3129 grid location points down to 3074 grid location points, which excluded points that contained any land data. The same process was repeated for each variable in Table 1. Basic regression statistics were performed for each variable downloaded and for each waterbody. These basic statistics were necessary to understand if and how the individual WBs changed over time and to see the rate of change, p-values, and R^2 values for those variables of interest.

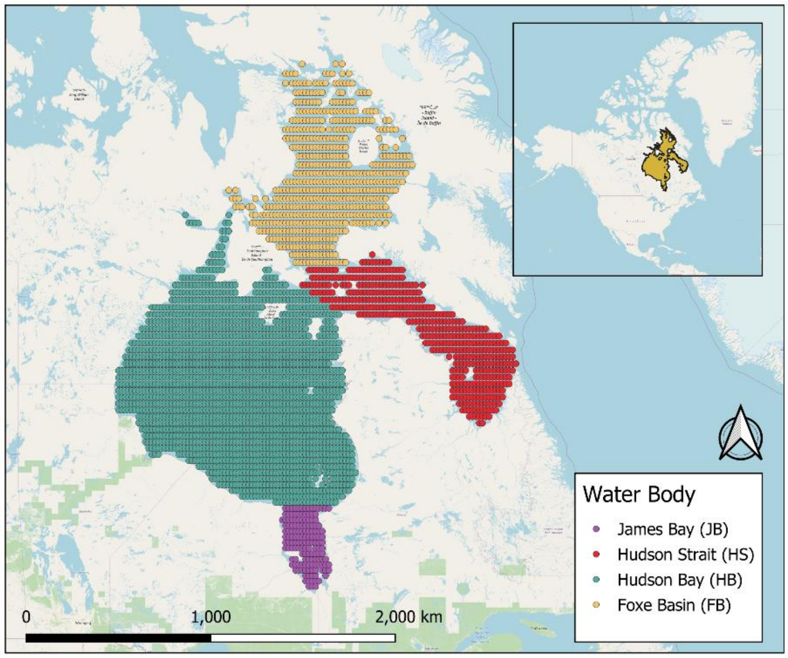

Figure 2 - Map of Study Area(s) including data points.

In the analysis which follows, the values for individual sub-basins are often merged into mean values for the Hudson Bay Complex (HBC) comprising all four water bodies. And, on specific occasions, into mean values for the Hudson Bay System (HBS) comprising FB, HB and JB without HS which is treated as a distinctive conduit for mass and energy transfer with the Labrador Sea. Because of the uniform longitudinal and latitudinal spacing of grid locations within the model domain, the number of grid locations per unit area varies within sub-basins owing to the convergence of meridians from south to north. The net effect results in a higher sample density of variables in FB than JB, for example. To avoid potential errors arising from taking the simple arithmetic mean of the sub-basins in determining the means for HBC and HBS, sub-basin means are weighted by their respective surface areas. These areas were determined manually by planimetering the area of each sub-basin in Google Earth Pro and then subtracting the planimetered area of prominent islands. The areal weightings shown in Table 2 thus represent the values for the marine system alone.

Table 2 - The surface water area, proportional area, sample size and model bathymetric depths for sub-basins within the Hudson Bay Complex and the Hudson Bay System.

ERA5 BATHYMETRY	AREA km^2	% HBC	% HBS	N	DEPTH m	MAX	MIN
HBC	1195433	100.0		3074	115	745	5
FB	180850	15.1	17.7	586	74	339	7
HB	772267	64.6	75.7	1863	121	268	11
HS	174470	14.6	0.0	481	166	745	5
JB	67746	5.7	6.6	144	32	57	10
HBS	1020863		100.0	2593	106	339	5

3.5 Data Analysis

3.5.1 Ice-Cover Seasons

Changes in the cryogenic cycle are identified using sea ice concentration (SIC) and sea ice extent (SIE) data. Note: Sea ice coverage is not referred to by the term SIE since, in the literature, SIE is calculated in km^2, whereas SIC is reported in percentages of other pixels. The phrase "sea ice coverage" is employed because ERA5 Sea-Ice Cover is reported in percentage terms to the presence or absence of ice at each grid location throughout the entire domain. Sea-ice extent represents the area of ice cover over the entire domain and can be expressed as a percentage of the total marine area. The connection between SIC, SIE, and albedo has been studied in-depth for the Arctic Ocean. For the purposes of this study, four ice-cover seasons, defined and listed in Table 2, are identified and referred to throughout the study.

This analysis proposes four ice-seasons based on these definitions and thresholds rather than defining them according to the calendar. The first is Ice-Free (IF), which happens when there is less than 10% snow or ice and over 90% open water on the surface. The second is the Ice-Covered (IC) season, when there is less than 10% open water while the ice may increase or decrease in thickness. However, due to the large number of leads and polynyas that arise and vanish periodically, HBC usually does not become fully ice-covered everywhere. Additionally, HBC doesn't experience 0% ice extent in a few years due a few locations where ice lingers into August and September, which are typically ice-free months, therefore a threshold of 5 persistent days of state change was employed to ensure the cells were classified correctly. A criterion of >90% was selected for the start of the IC season to take these into consideration. The entire IC season continues into the first few months of the following calendar year. The third ice-season is defined as the "freeze-up" (FU) corresponding to the end of the IF season and the beginning of the IC1 season. Ice cover rapidly increases over this period. This season is defined by an ice-coverage criteria that starts at >10% and extends up to 90%. Lastly when ice begins to thin to the point that it separates from the main ice pack developing areas of open water this marks the beginning of the break-up (BU) season. It ends when the water body is ice-free. This season is defined as having ice extent below 90% and above 10%.

Table 3 - Names, Thresholds, and Definitions of Ice Seasons.

Season	**Definition**	**Ice-Coverage Threshold (%)**
Ice Free	Almost complete absence of ice.	10<
Freeze-Up	"Mixed" state transitioning from complete absence of ice to almost complete ice cover.	10 < Ice-Cover < 90
Break-Up	"Mixed" state transitioning from complete almost complete ice cover to complete absence of ice.	10 > Ice-Cover > 90
Ice Covered	Almost completely covered in ice.	>90

3.5.2 Energetics

Surface Radiation Budget

The surface radiation balance describes the net radiation on a two-dimensional plane of zero thickness at the surface accounted by the incoming and outgoing fluxes of radiation ($MJ/m^2/d$). It is described as:

$$Q^* = (K\downarrow - K\uparrow) + (L\downarrow - L\uparrow) \quad (1)$$

or

$$Q^* = (K^*) + (L^*) \quad (2)$$

where Q* — net all-wave radiation, K↓ — incoming shortwave radiation, K↑ — reflected shortwave radiation, L↓ — incoming longwave radiation, L↑ — outgoing longwave radiation which is given by the Stefan-Bolzmann Law $L\uparrow = \varepsilon\sigma T_0^4$ where ε is the surface emissivity, σ is the SB constant and T_0 is the surface temperature (K) and K* is the net shortwave radiation where $K^* = K\downarrow(1-\alpha)$ where α is the surface albedo. The combined absorbed short- and long-wave radiation at the surface ($K^* + L\downarrow$) is often referred to as the surface radiative forcing.

Surface Energy Budget

The surface energy budget accounts for the partitioning of energy inputs and outputs from the plane which is the sea surface in this study. A balance exists between the vertical radiative energy inputs from above plus vertical precipitation energy inputs from above. These will balance the net vertical convective losses of energy to the atmosphere in the form of sensible heat and latent heat (evaporation), and vertical losses of energy downward into the subsurface containing the water or ice below. (J/m^2/s or W/m^2) or (MJ/m^2/d) The surface energy budget can be expressed as:

$$Q^* + Q_P + Q_H + Q_E - Q_S = 0 \quad (3)$$

where Q_H — sensible heat flux, Q_E — latent heat flux, Q_S— subsurface or ocean heat flux (positive directed downwards away from the surface), and Q^* is the net radiation and $Q_P = Q_{SH} + Q_{Lf}$ is the precipitation flux (positive directed towards the surface) and Q_{SH} is sensible heat transfer from precipitation and Q_{Lf} is the latent heat release from melting snow. By rearranging (3) a solution for the energy gained or lost by the ocean surface can be solved for as,

$$Q_S = Q^* + Q_P + Q_H + Q_E \quad (4)$$

Here, the convective fluxes of sensible and latent heat are considered negative away from the surface and are dependent on the turbulent transfer coefficients and respective vertical temperature and vapour pressure gradients. Energy is also transferred to the surface via precipitation from the atmosphere. Although consideration of precipitation is a fundamental component of the surface water balance, falling rainfall also transfers energy to the surface when it is warmer than the surface and cools upon contact. The reverse occurs when falling rain is cooler than the surface whereby it extracts surface energy upon warming as it makes contact. The magnitude of this energy flux depends dually on the mass flux of rain (kg/m^2/d = mm/d) and the temperature difference between the rain and surface ($T_P - T_0$).

For snow, there is an additional energy flux due to the latent heat of fusion, Lf (0.334 MJ/kg). Latent energy realized as an energy gain in the atmosphere during the freezing process in the formation of snow, is realized as an energy loss at the surface in the melting process. This flux is also dependent on the mass flux of snow but rather than being realized as an instantaneous energy loss, it is realized by the surface only during the change of state (i.e., during melt). As is the case with the impact of snowfall on the surface water budget in generating runoff, the surface will only realize the latent energy removal during periods when energy which would otherwise be available for other processes is consumed in melt. Consequently, the impact of precipitation energy inputs to the surface depends on the integration time. Daily, their influences may be negligible relative to radiative or convective fluxes but on a seasonal or annual basis, they may be more influential. When integrated over an entire cryogenic cycle, all snow residing on the ice surface will contribute to an extraction of energy from the surface. Over the year some snow mass will be lost because of snow evaporation or sublimation Therefore ERA5 annual losses due to snow evaporation are subtracted from gross snowfall amounts to derive the net latent heat of fusion component (Q_{Lf}) of the surface energy budget. Snow residing on the surface is also influenced by lateral redistribution (drifting) between grid locations. Because this analysis focusses on the bulk characteristics of an entire water body, these redistribution effects are assumed to be cancelling and therefore negligible.

Q_S represents the net energy exchange between the atmosphere and the sea surface, the top plane of a column of water extending to the seafloor. Positive values of Q_S contribute to water warming or ice melt, with negative values contributing to water cooling or ice growth. The spatial and temporal variations in these energy flows are the principle focus of this thesis. ERA5 provides daily estimates of all the radiation budget components, as well as the convective fluxes of sensible and latent heat. Daily rainfall is computed from the difference between daily precipitation (m/day) and snowfall (snow water equivalent, SWE, m/day) components. Precipitation temperatures are assumed to correspond to the daily air temperatures at 2 m height and surface temperatures are also provided. All the daily values required to solve for Q_S in (4) are summed for each entire year over 45 years at 3074 locations and presented in the next chapter with a focus on temporal trends over the study period and interannual variability to contextualize and highlight the important factors responsible for changes in surface energy exchange and sea ice in the Hudson Bay Complex.

It is important, however, to highlight some additional factors which may contribute to the thermal response of the water column. A water column may exchange energy across the five other faces other than the surface. As a moving fluid, sensible and latent energy (ice) may be transported into or out of the volume laterally affecting its thermal response. When more energy is being transported in across one face laterally than is being transported out the downstream face, then the lateral energy convergence will warm the volume. Lateral energy divergence will contribute to cooling. These factors could be large relative to the surface energy exchange particularly where grid cells are in zones of persistent ocean currents or steep horizontal temperature gradients. This could, for example, result in any given location cooling faster or slower than the surface energy budget would suggest. These effects are scale dependent. For example, in an entirely closed system, zones of lateral divergence and convergence will offset each other. In the HBC as whole, this is an approximation which is assumed here. Under steady state conditions, the annual values of Q_s should approximate zero in a perfectly closed system. Over 45 years, the extent to which annual Qs deviates from zero should reveal how lateral transport across the boundaries of the system compares to the magnitude of the vertical transport within the system. For the Hudson Bay Complex, these unaccounted-for sub-surface annual energy fluxes likely arise from river discharge into the Bay, current flow through Fury and Hecla Strait into Foxe Basin and the net flow of freshwater out through Hudson Strait. However, the net flow out through Hudson Strait is very complex due to counterflowing currents.

Lastly, there may also be energy exchange across the base of the water column. When the thermally active water column extends to the ocean floor, then the potential exists for geothermal exchange of heat contributing to the thermal response of HBC over a 45-year period. More typically, the base of the thermally active water column extends to the base of the mixed layer during the ice-free season which is defined by a thermocline. The mixed layer is, by definition, a layer which undergoes turbulent mixing and within which energy is readily redistributed. In other seasons, the surface mixed layer breaks down, and mixing may well extend to the seafloor owing to wind-driven effects and semi-diurnal tidal influences. ERA5 does not provide daily values of water temperature at fixed depths other than at the surface itself and therefore we must treat the actual annual changes in the thermal behaviour of the entire water column within the HBC over time as an approximation.

Chapter 4 – Results

4.1 Water Budget

The Hudson Bay Complex (HBC) water budget shifted noticeably over the 45-year period from 1980 to 2024. Both evaporation and precipitation increased significantly, but evaporation exhibited a stronger positive trend. Evaporation rose at a rate of 1.32 mm yr^{-1} ($p < 0.001$), while precipitation increased at 0.99 mm yr^{-1} ($p < 0.05$). The net balance (P–E) showed no significant long-term trend, reflecting the near-equivalent rates of increase in inputs and outputs, although interannual variability remained pronounced (Figure 3).

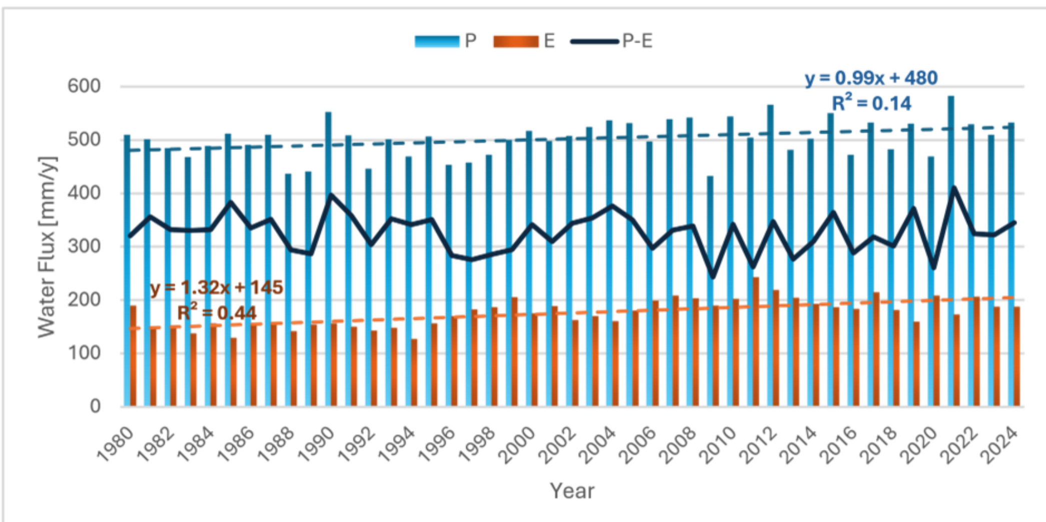

Figure 3 - Annual water budget components for the Hudson Bay Complex from 1980 to 2024. Bars represent precipitation (P, blue) and evaporation (E, orange), while the black line indicates the net balance (P–E). A significant increasing trend is observed for precipitation ($p< 0.05$; R^2:0.14) and evaporation ($p < 0.001$, R^2:0.44), whereas the P–E balance exhibits no significant trend.

4.2 Precipitation, Rainfall, and Snowfall

Precipitation exhibited spatially heterogeneous trends across the four major waterbodies. FB, HS, and JB all showed significant increases in annual precipitation at rates of 1.4 mm yr^{-1}, 1.1 mm yr^{-1}, and 1.7 mm yr^{-1}, respectively ($p < 0.05$). HB, in contrast, displayed no statistically significant trend ($p > 0.05$) (Figure 4a).

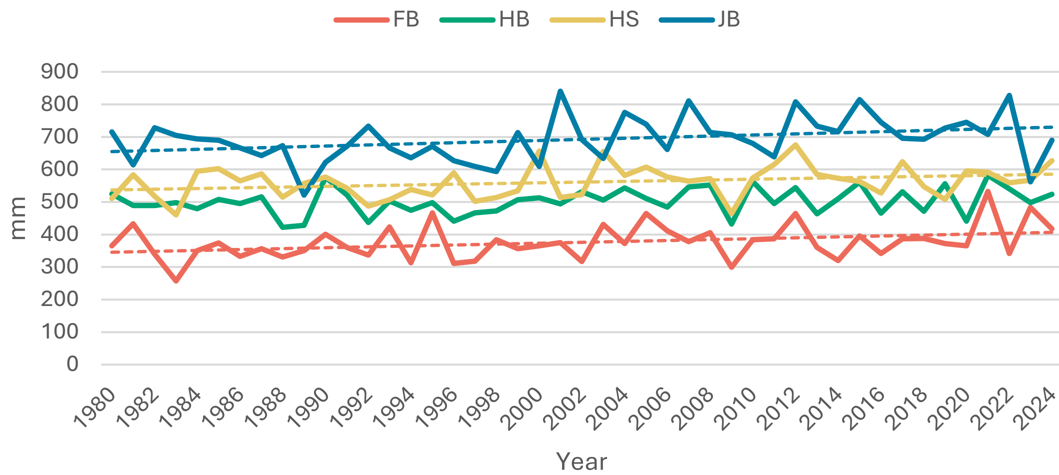

Figure 4a - Annual precipitation (mm) for each of the four main waterbodies from 1980 to 2024. A significant increasing trend is observed for FB ($p < 0.05$; R^2:0.12), HS ($p < 0.05$; R^2: 0.09), and JB ($p < 0.05$; R^2: 0.11), whereas HB exhibits no significant trend ($p > 0.05$).

Rainfall trends were more uniform, with all four waterbodies showing significant increases. FB rainfall rose at 1.3 mm/y, HB at 1.0 mm/y, HS at 1.1 mm/yr, and JB at 1.6 mm/y. These trends were significant at $p < 0.05$ for FB, HS, and JB, and $p < 0.01$ for HB (Figure 4b).

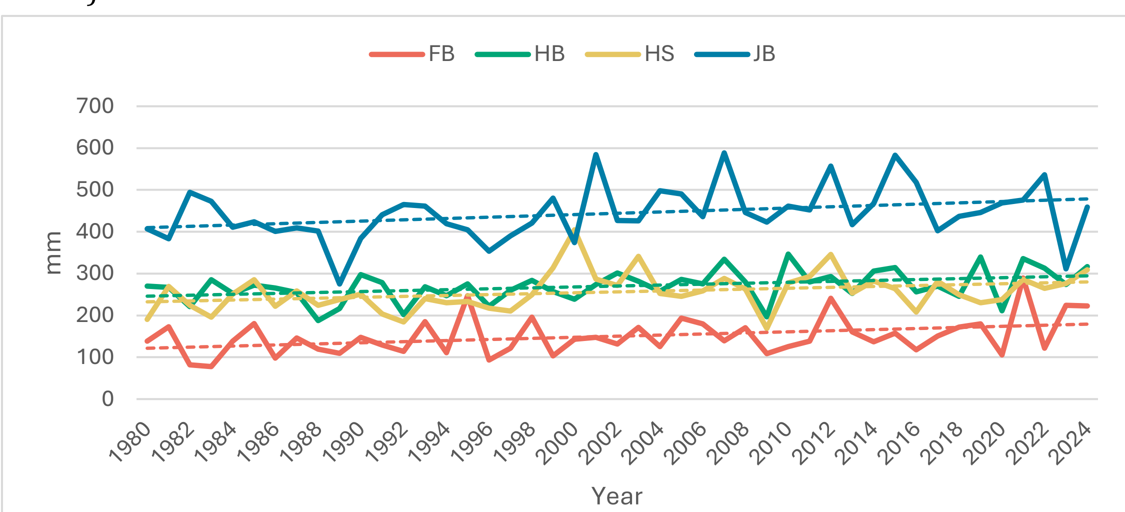

Figure 4b - Annual rainfall (mm) for each of the four main waterbodies from 1980 to 2024. A significant increase trend is observed for FB (R^2: 0.14), HS (R^2:0.10), and JB (R^2: 0.10) at $p < 0.05$, and significant at $p < 0.01$ for HB (R^2:0.15).

Snowfall, expressed in snow water equivalent (SWE), exhibited no significant long-term change across the basin. FB, HS, and JB showed slight but statistically insignificant increases, while HB displayed a weak negative trend (Figures 3 and 4c).

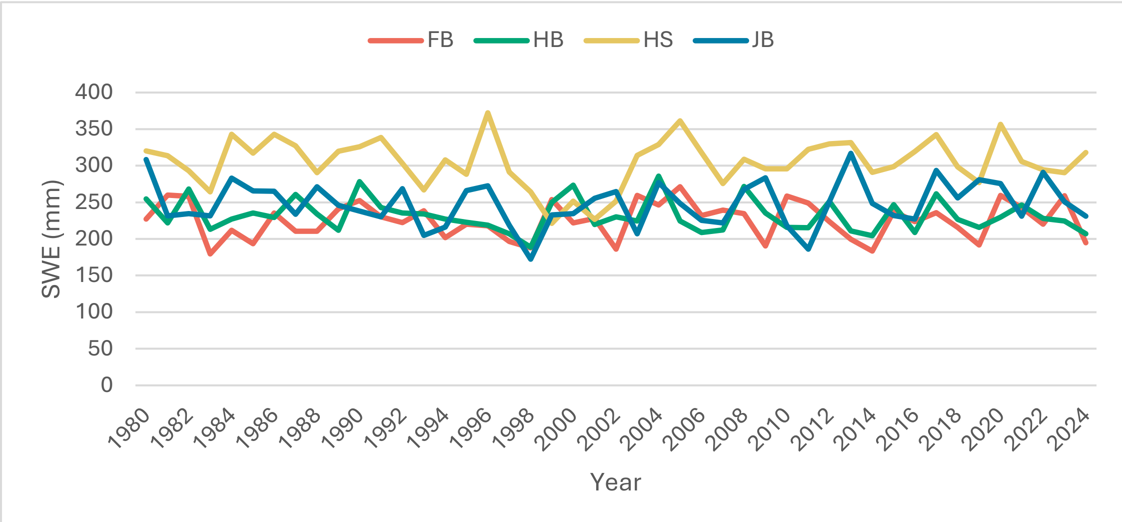

Figure 4c - Annual snowfall (mm SWE) for each of the four main waterbodies from 1980 to 2024. FB, JB, and HS experience a slight increase in snowfall over the period of study, but HB experiences a slight decrease. None of the waterbodies exhibit any significant trend ($p > 0.05$).

4.3 Surface and Air Temperature

Analysis of both air and surface temperatures from 1980 to 2024 revealed consistent warming trends across all four study sites (FB, HB, HS, and JB), with comparable results across both datasets (Figs. 5a and 5b). Linear regression indicated positive temperature trends at all locations, with slopes ranging from 0.067 to 0.093 °C yr^{-1}. JB exhibited the steepest and most robust warming (0.080–0.093 °C yr^{-1}) while HB and HS showed intermediate rates (0.069 – 0.074 °C yr^{-1}). FB, though initially the coldest site, also demonstrated a clear warming trajectory (0.067 – 0.071 °C yr^{-1}). Despite interannual variability, particularly at JB, the overall long-term signal was one of sustained warming. By the early 2020s, mean winter temperatures had increased by approximately 2–4 °C relative to the early 1980s baseline, indicating a spatially but site-specific pattern of regional climate warming.

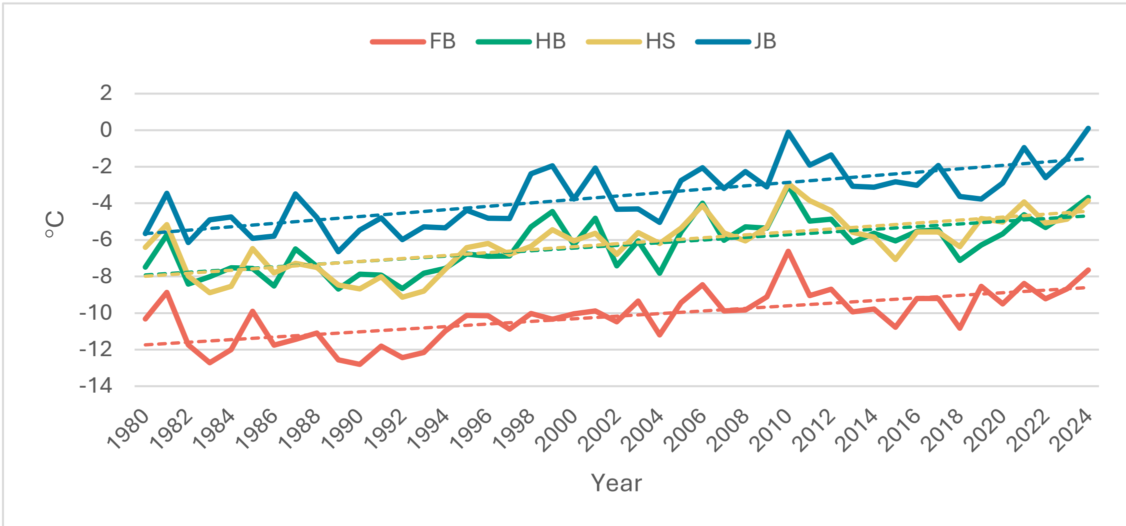

Figure 5a - Annual mean surface temperature (°C) for each of the four main waterbodies from 1980 to 2024. A significant increasing trend is observed for all waterbodies FB (R^2: 0.45), HB (R^2: 0.45), HS (R^2: 0.49), and JB (R^2: 0.55) at $p < 0.001$.

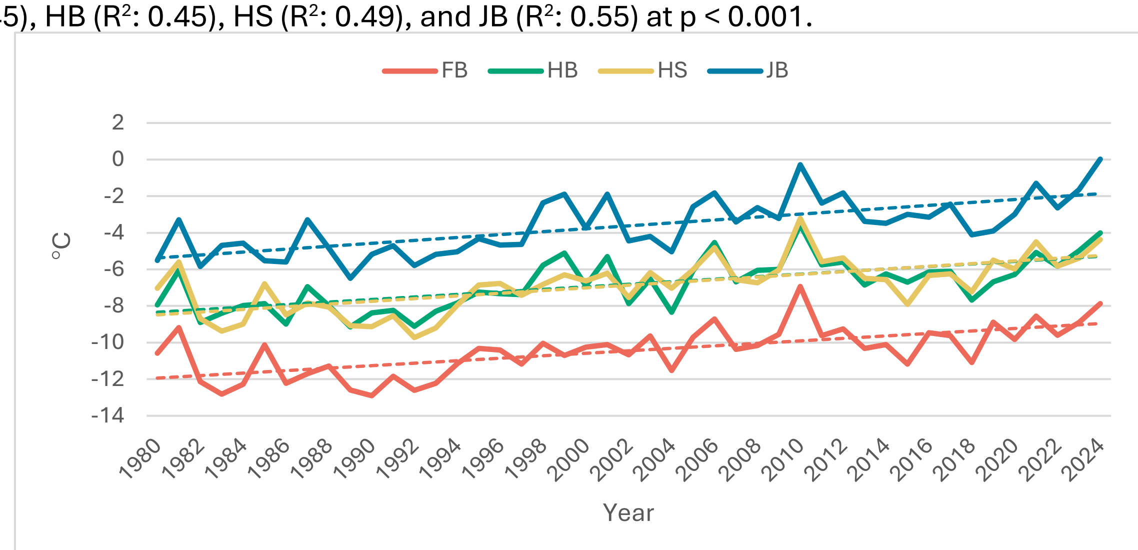

Figure 5b - Annual mean air temperature (°C) for each of the four main waterbodies from 1980 to 2024. A significant increasing trend is observed for all waterbodies FB (R^2: 0.43), HB (R^2: 0.43), HS (R^2: 0.44), and JB (R^2: 0.47) at $p < 0.001$.

Analysis of temperature gradients and seasonal metrics from 1980 to 2024 revealed significant long-term warming trends across the study region (Fig. 6a). All temperatures displayed positive linear slopes, indicating an increase over time. Maximum (T_0 max) and minimum (T_0 min) annual temperatures showed significant increases of 0.073 °C yr^{-1} and 0.120 °C yr^{-1}, respectively. Annual air temperatures (T_2) also warmed at 0.076 °C yr^{-1}. Despite interannual variability, the consistent positive slopes across all indices highlight a robust regional warming signal.

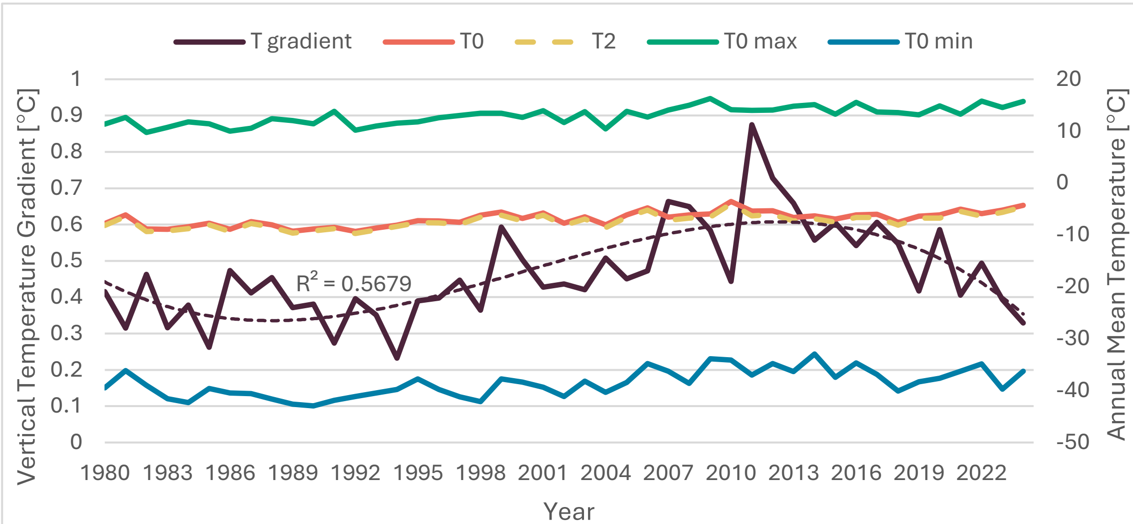

Figure 6a - Temperature gradient (T_0-T_2, °C) and temperatures for the entire HBC from 1980 to 2024. A significant increasing trend is observed for all temperatures, T_0 (R^2: 0.50), T_{0max} (R^2: 0.58), T_{0min} (R^2: 0.37), and T_2 (R^2: 0.46), at $p < 0.001$.

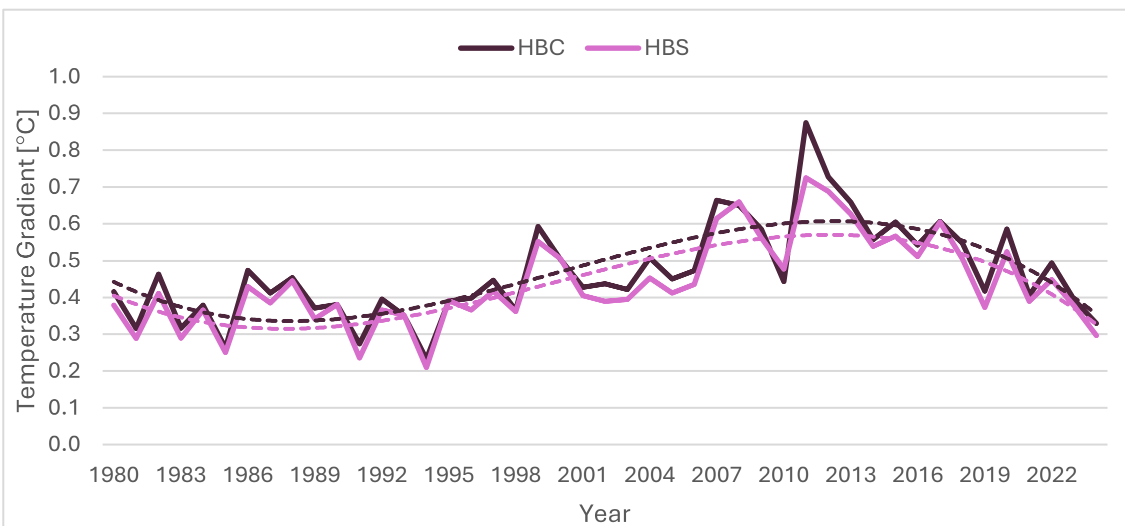

Figure 6b – Vertica; temperature gradient (T_0-T_2: °C) for the HB (R^2: 0.57) and HBS (R^2: 0.60) from 1980 to 2024. Dotted lines represent best-fit 3rd order polynomials.

Both HBC (encompassing all sub-basins) and HBS (excluding HS) exhibited warming, with regression slopes of 0.087 °C yr^{-1} and 0.089 °C yr^{-1}, respectively. The close agreement in slopes across subregions suggests that warming is spatially coherent across the basin, with no single subregion driving the trend. Figure 6b indicates that, initially, lapse temperature gradients showed little change or exhibited a slight decline. However, a pronounced increase is observed following the eruption of Mount Pinatubo in 1992, continuing until approximately 2012, after which the temperature gradients begin to decline once more. This non-linear pattern persists with and without the inclusion of Hudson Strait.

4.4 Seasonal Durations and Sea-Ice Cover

Ice phenology demonstrated lengthening of the open-water (OW) season and shortening of the ice-covered (IC) season across all study sites (Figures 7a–e). These shifts correspond to pronounced declines in mean annual sea-ice cover. From 1980 to 2024, annual mean sea-ice extent decreased significantly across FB, HB, HS, JB, and HBC, with regression slopes ranging from –0.21% yr^{-1} (HS) to –0.40% yr^{-1} (JB). Season lengths for the five waterbodies (FB, HB, HS, JB, HBC) varied systematically for the four seasons (IC, BU, OW, FU) in the study area. Summary statistics, significance, and model fit are presented in Tables 4 and 5.

Season lengths varied consistently. For the IC season, FB averaged 129 ± 30 days, HB 112 ± 25 days, HS 108 ± 29 days, JB 107 ± 27 days, and HBC 118 ± 31 days, representing the longest durations. All IC durations were significantly longer than those in BU ($p < 0.01$ for all variables) and OW ($p < 0.05$ for FB, HB, and HBC). For the BU season, mean durations were FB: 78 ± 22 days, HB: 66 ± 19 days, HS: 85 ± 24 days, JB: 64 ± 21 days, and HBC: 73 ± 23 days, significantly shorter than IC ($p < 0.01$), but some variables (FB, HBC) were longer than FU ($p < 0.05$), reflecting intermediate season length. The OW season exhibited intermediate season lengths: FB 92 ± 25 days, HB 84 ± 22 days, HS 96 ± 28 days, JB 78 ± 21 days, and HBC 85 ± 24 days. Compared to IC, FB, HB, and HBC were significantly shorter (p = 0.02 to 0.03), while HS and JB were not significantly different ($p > 0.05$). OW did not differ significantly from BU ($p > 0.05$). FU consistently showed the shortest seasonal durations, with FB 62 ± 20 days, HB 59 ± 18 days, HS 64 ± 21 days, JB 58 ± 19 days, and HBC 61 ± 20 days, significantly shorter than all other seasons ($p < 0.001$).

The overall trends showed that, across both phenological metrics, IC maintained the longest seasons, FU had the shortest seasons, and OW and BU consistently occupied intermediate positions. These patterns demonstrate strong, condition-dependent shifts in duration of seasonal activity across the Hudson Bay study area (Figures 7a-e, Table 4).

Table 4 - Regression Statistics for Mean Season Lengths ± SD, p-values, and R^2.

Variable	**IC Days**	**BU Days**	**OW Days**	**FU Days**	**p-value**	**R^2**
FB	129 ± 30	78 ± 22	92 ± 25	62 ± 20	<0.001	0.70
HB	112 ± 25	66 ± 19	84 ± 22	59 ± 18	<0.001	0.68
HS	108 ± 29	85 ± 24	96 ± 28	64 ± 21	<0.001	0.69
JB	107 ± 27	64 ± 21	78 ± 21	58 ± 19	<0.001	0.65
HBC	118 ± 31	73 ± 23	85 ± 24	61 ± 20	<0.001	0.70

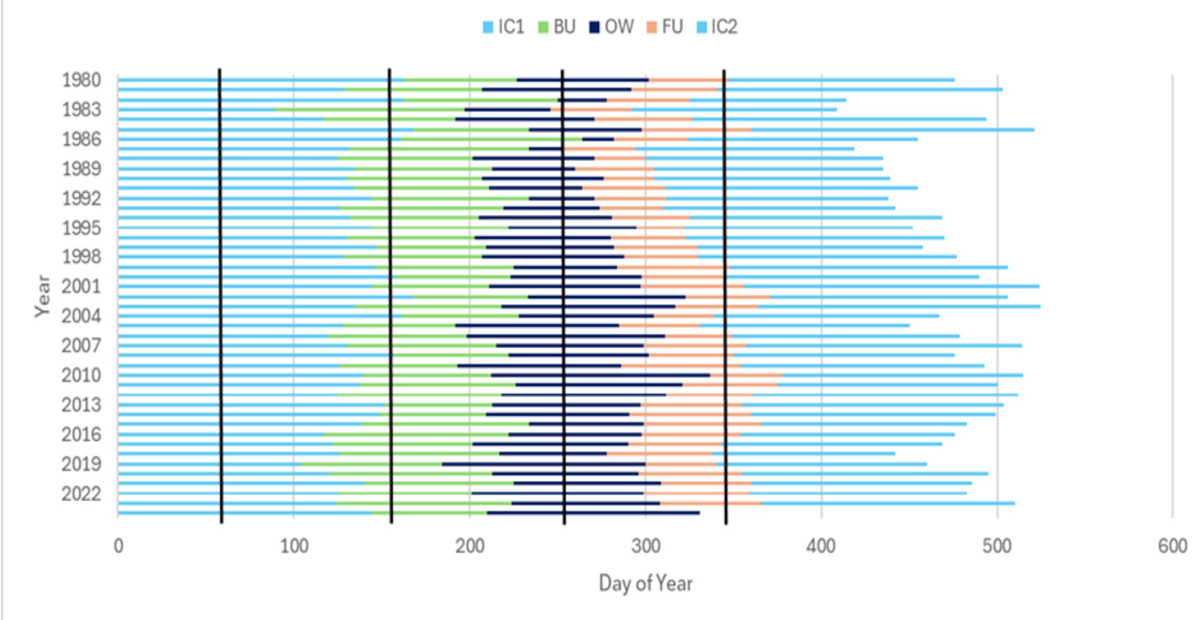

Figure 7a - Cryogenic year of FB from 1980 - 2024. Where light blue shows the IC season, greens show the BU season, navy shows the OW season, orange is the FU season, and light blue is the IC seasons. The vertical black bars represent the equinoxes and solstices. The first light blue bar shows the length of the IC season since DOY 1. The second light blue bar shows the length of the IC season extending into the next year.

Figure 7b - Cryogenic year of HB from 1980 - 2024. Where light blue shows the IC season, greens show the BU season, navy shows the OW season, orange is the FU season, and light blue is the IC seasons. The vertical black bars represent the equinoxes and solstices. The first light blue bar shows the length of the IC season since DOY 1. The second light blue bar shows the length of the IC season extending into the next year.

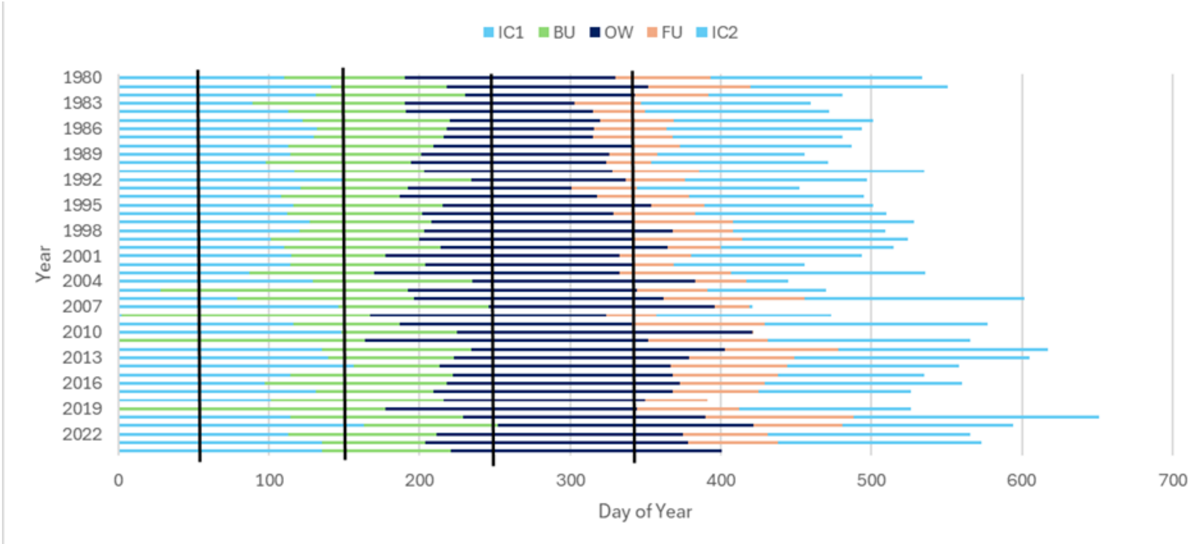

Figure 7c - Cryogenic year of HS from 1980 - 2024. Where light blue shows the IC season, greens show the BU season, navy shows the OW season, orange is the FU season, and light blue is the IC seasons. The vertical black bars represent the equinoxes and solstices. The first light blue bar shows the length of the IC season since DOY 1. The second light blue bar shows the length of the IC season extending into the next year.

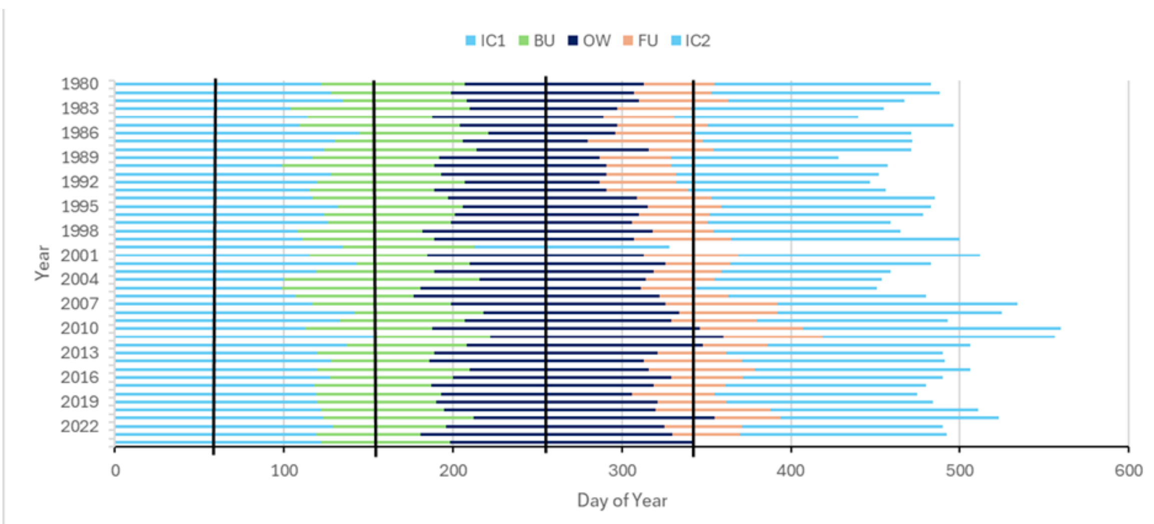

Figure 7d - Cryogenic year of JB from 1980 - 2024. Where light blue shows the IC season, greens show the BU season, navy shows the OW season, orange is the FU season, and light blue is the IC seasons. The vertical black bars represent the equinoxes and solstices. The first light blue bar shows the length of the IC season since DOY 1. The second light blue bar shows the length of the IC season extending into the next year.

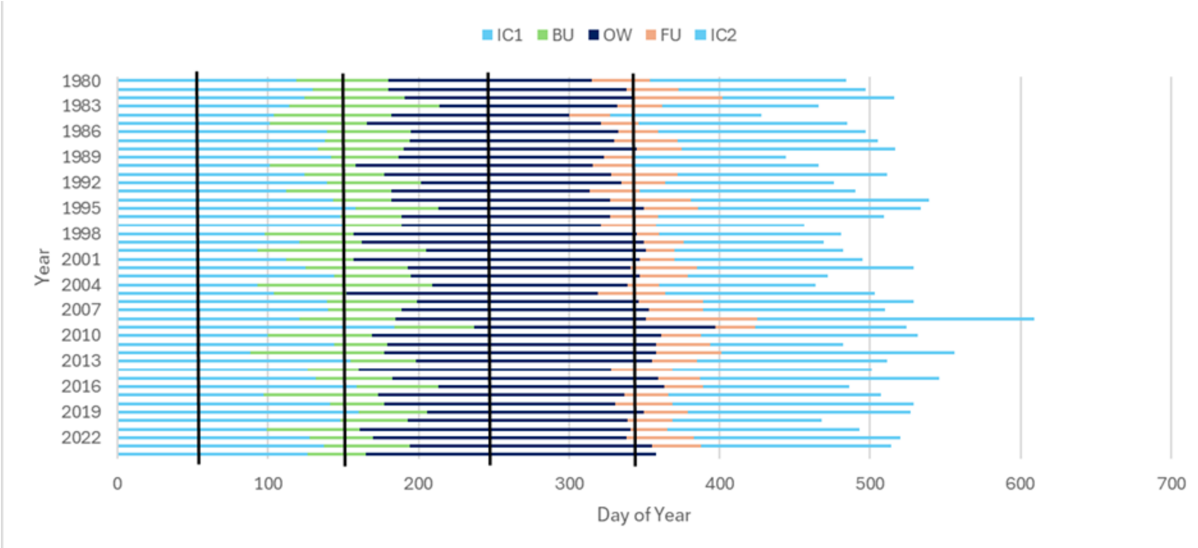

Figure 7e - Cryogenic year of HBC from 1980 - 2024. Where light blue shows the IC season, greens show the BU season, navy shows the OW season, orange is the FU season, and light blue are the IC seasons. The vertical black bars represent the equinoxes and solstices. The first light blue bar shows the length of the IC season since DOY 1. The second light blue bar shows the length of the IC season extending into the next year.

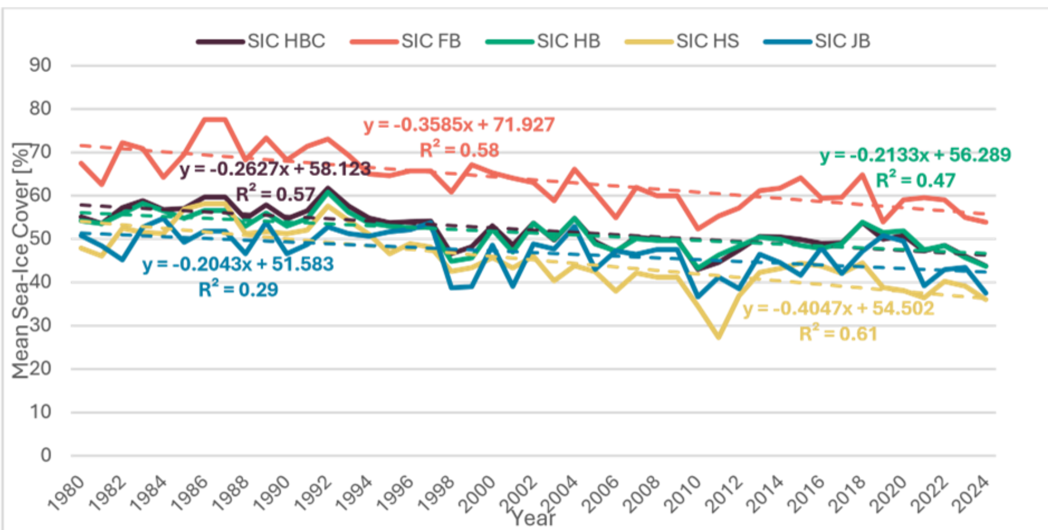

Figure 8 - Sea-Ice Cover (%) for each of the four waterbodies FB, HB, HS, and JB, and the combined waterbody of HBC. All waterbodies show significant changes ($p < 0.001$).

Figure 8 shows the lowest annual SIC occurring on Hudson Strait because of it experiencing the most rapid decline of 4% per decade. The rate of decline has been almost matched on FB at 3.6% per decade which has the consistently highest ice-cover over the study period. The other two sub-basins have experienced intermediate rates of decline between 2.0 and 2.6% per decade and are also highly significant at $p < 0.001$. Nevertheless, interannual SIC variability has been quite large ($0.29 < R^2 < 0.61$). Mean annual ice-cover still hovers slightly below 40% in 2024 even in JB and HS while the absolute minima occurred 14 to 15 years earlier in 2010 and 2011 and comparable minima occurred in 1998 and 1999. By maintaining persisting trends, linear extrapolation would suggest ice-free conditions not arriving until between 2114 and 2181 for Hudson Strait and Foxe Basin respectively.

4.5 Radiation Fluxes

Net shortwave radiation increased significantly in all subregions. FB, HB, HS, and HBC with highly significant increases ($p < 0.001$), while JB also rose significantly ($p < 0.01$) (Figure 9). Conversely, incoming shortwave radiation (insolation) exhibited no significant long-term change in any region (Figure 10).

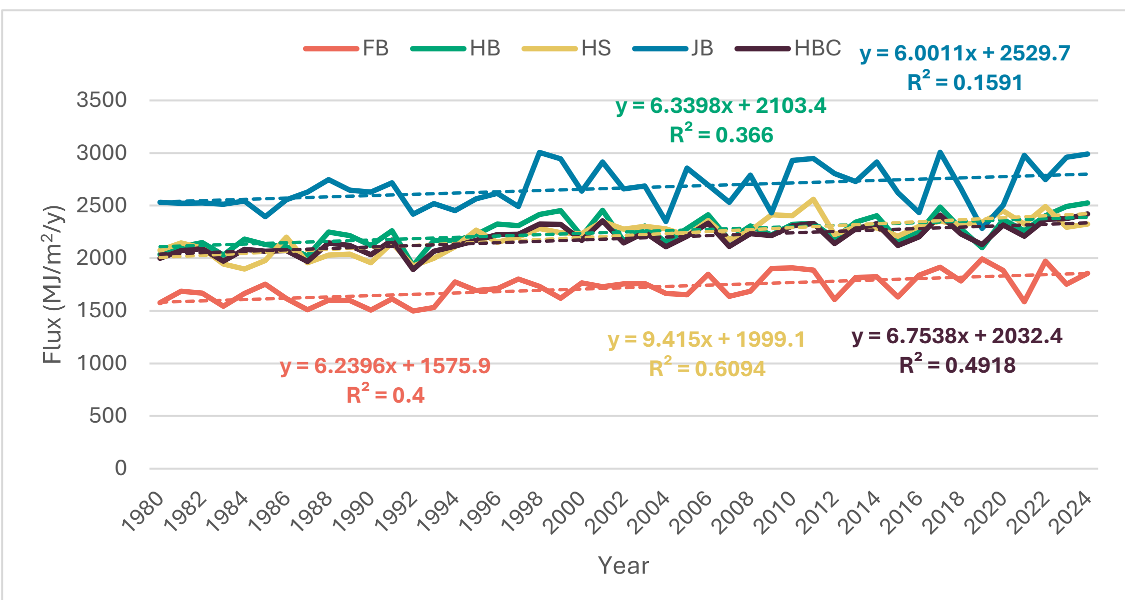

Figure 9 - Annual net shortwave radiation ($MJ/m^2/y$) from 1980 to 2024 across the five waterbodies (FB, HB, HS, JB, and HBC). Statistically significant trends observed in all waterbodies; FB, HB, HS, and HBC at $p < 0.001$, and JB at $p < 0.01$.

Net longwave radiation provides radiative surface cooling offsetting shortwave warming. It became increasingly negative in HB, JB, HBC, and HS ($p < 0.001$ for HB, JB, HBC; $p < 0.01$ for HS) indicating that the upward flux in increasing faster than the incoming flux. The FB trend is not statistically significant. There is considerable interannual variability superimposed on the trends (HBC $R^2 = 0.39$), (Figure 11). Over the study period, HBC net longwave radiation averaged -1287 MJ/m^2/y, partially offsetting shortwave absorption of 2188 MJ/m^2/y, providing a net radiative surplus at the sea surface of 900 MJ/m^2/y annually.

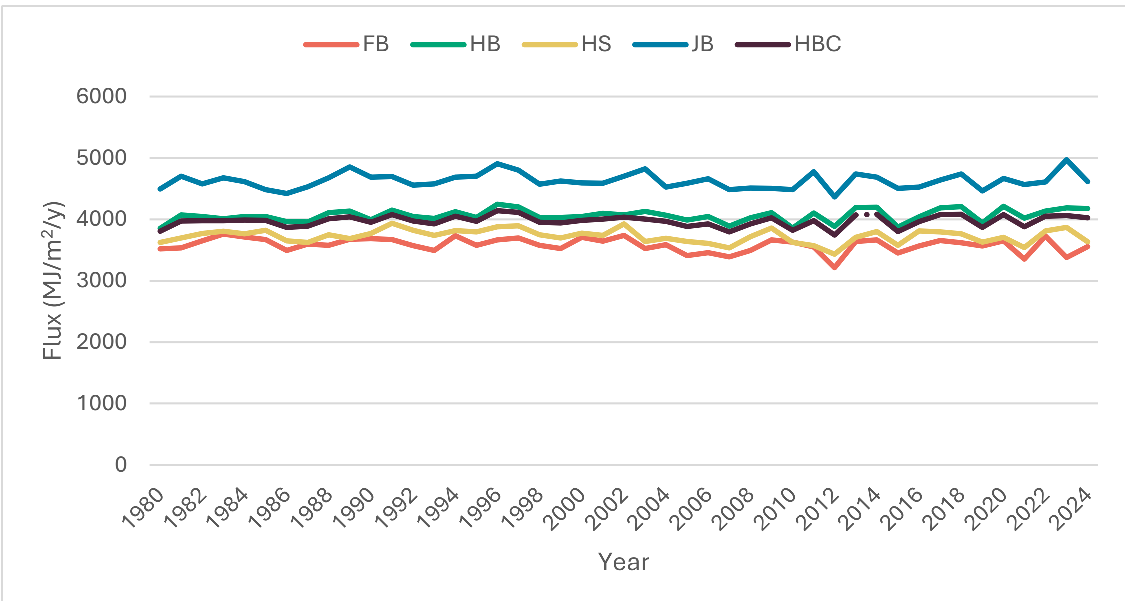

Figure 10 - Annual incoming shortwave radiation (insolation in MJ/m^2/y) from 1980 to 2024 across the five waterbodies (FB, HB, HS, JB, and HBC). No significant trends were observed for any of the waterbodies.

Incoming longwave radiation increased significantly across all regions ($p < 0.001$) (Figure 12).

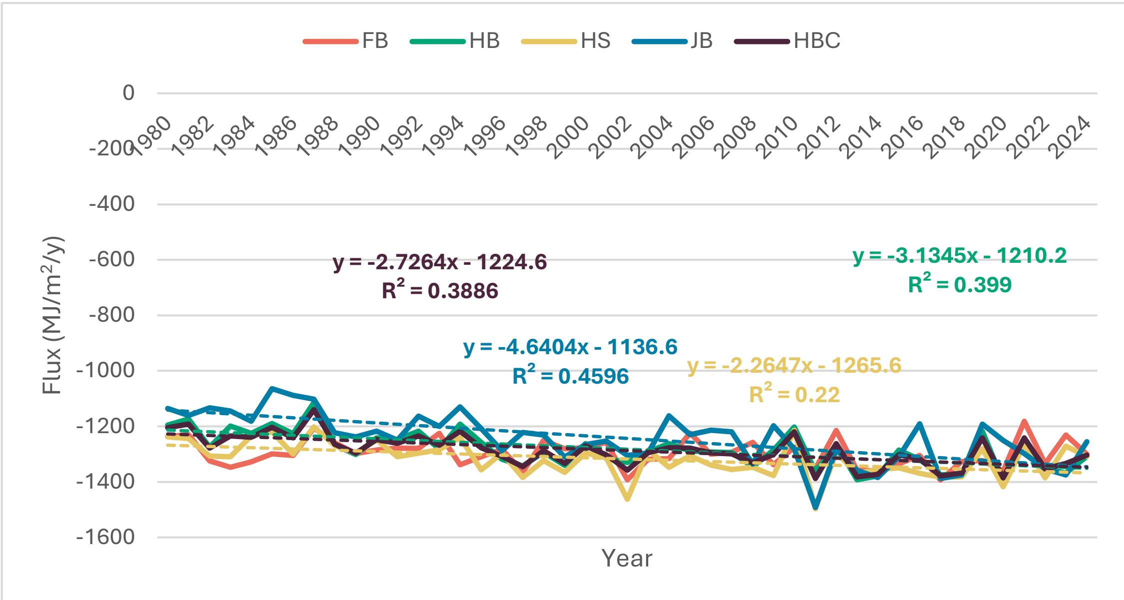

Figure 11 - Annual net longwave radiation (MJ/m²/y) from 1980 to 2024. Statistically significant trends observed for HB ($p < 0.001$), JB ($p < 0.001$), HBC ($p < 0.001$), and HS ($p < 0.01$); no significant trend observed in FB.

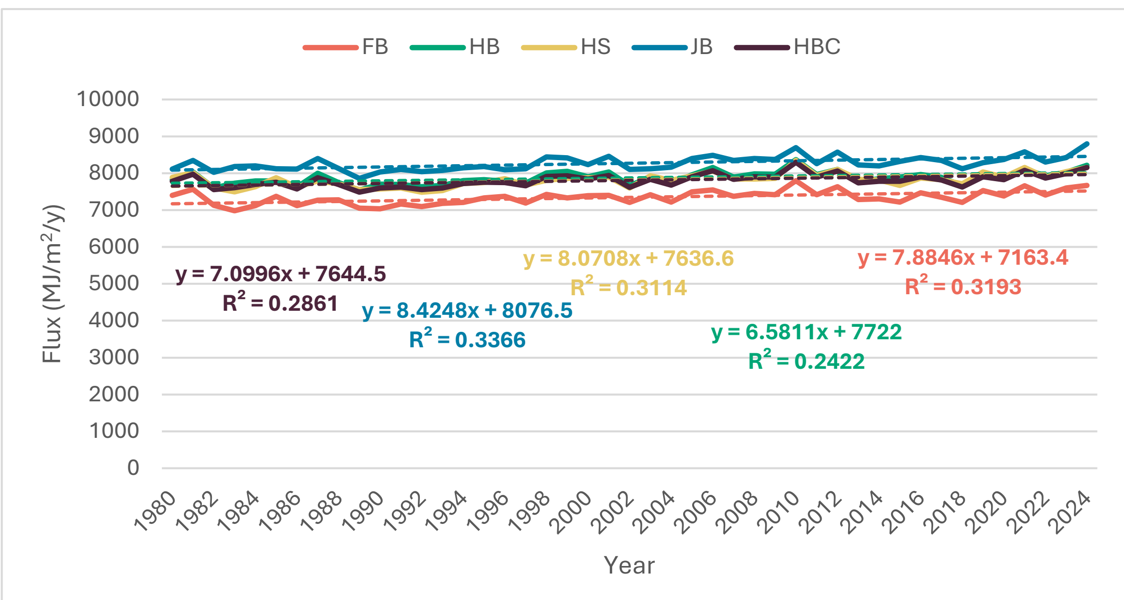

Figure 12 - Annual incoming longwave radiation (MJ/m²/y) from 1980 to 2024 across the five waterbodies (FB, HB, HS, JB, and HBC). All waterbodies experience statistically significant trends at $p < 0.001$.

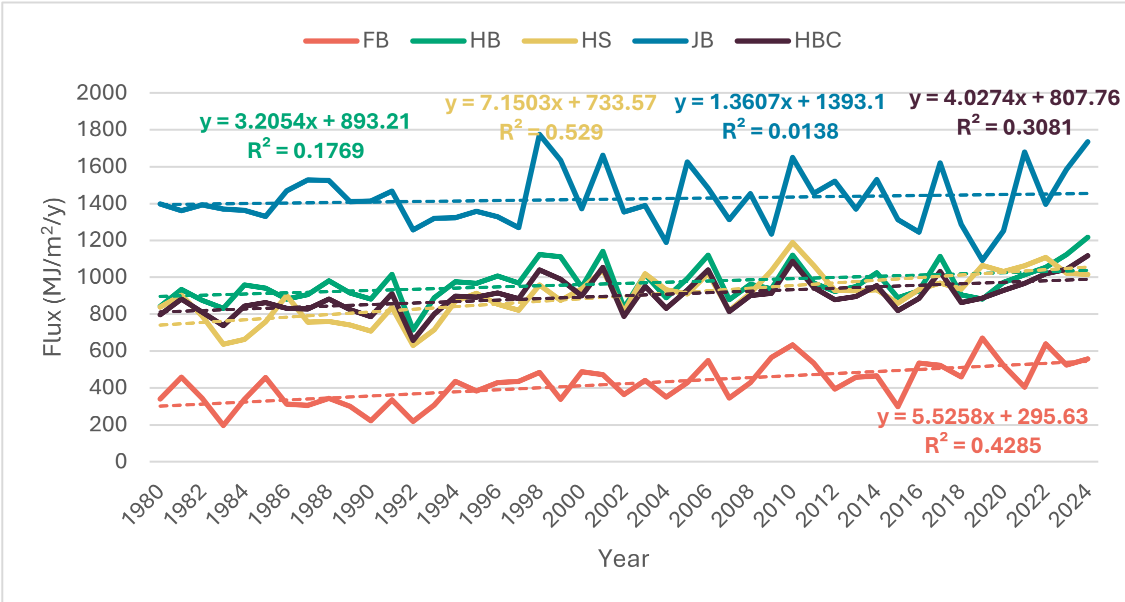

Figure 13 - Annual net radiation (MJ/m²/y) from 1980 to 2024 across the five waterbodies (FB, HB, HS, JB, and HBC). JB is insignificant; FB, HS, HB, and HBC are significant at $p < 0.001$.

Net radiation increased significantly in FB, HS, HB, and HBC ($p < 0.001$), while JB showed no significant trend (Figure 13).

Radiative forcing (K* + L↓) across all sub-basins (Figure 18a-d) showed a robust positive trajectory over the study period, with a significant increase in contributions from both shortwave and longwave components ($p < 0.001$). For HBC (Figure 18e) the total combined radiative inputs (K* + L↓) increased at 13.85 MJ m^{-2} yr^{-1} while incoming longwave (L↓) and net shortwave (K*) fluxes increased at 6.75 MJ m^{-2} yr^{-1} and 7.10 MJ m^{-2} yr^{-1}, respectively (Figures 18a–d). These findings confirm a basin-wide increase of radiative energy inputs, near-equally driven by greenhouse effects and ice-albedo feedback promoting ocean warming over the study period.

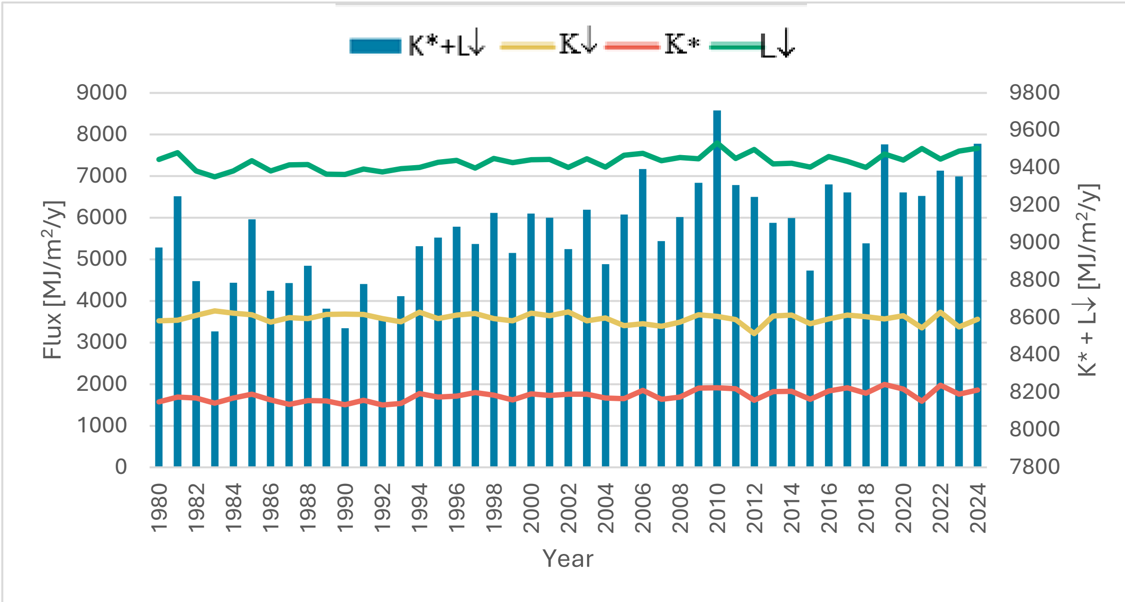

Figure 14a - Radiative forcing components of FB from 1980 to 2024 ($p<0.001$). Insolation (K↓) is shown for reference. ($p > 0.05$)

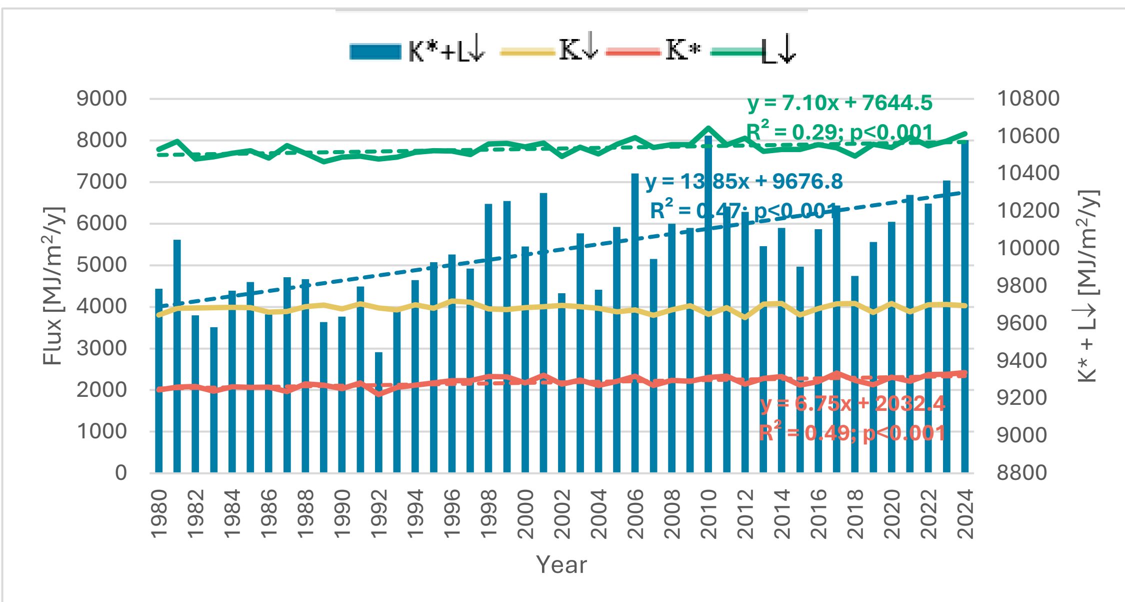

Figure 14b - Radiative forcing components of HB from 1980 to 2024 ($p<0.001$). Insolation (K↓) is shown for reference.

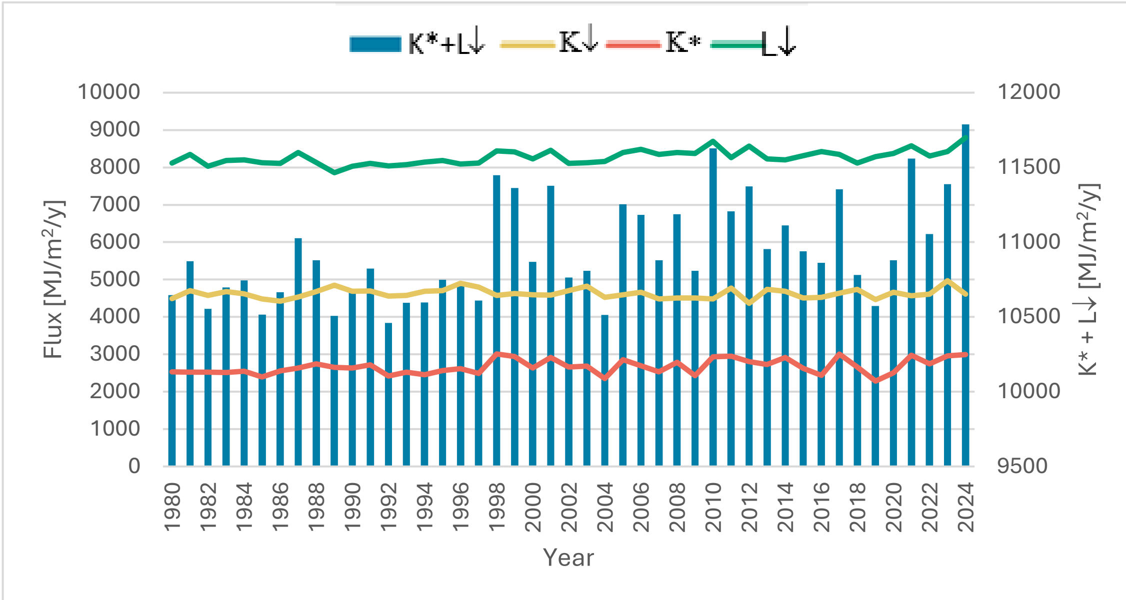

Figure 14c - Radiative forcing components of HS from 1980 to 2024 ($p<0.001$). Insolation (K↓) is shown for reference.

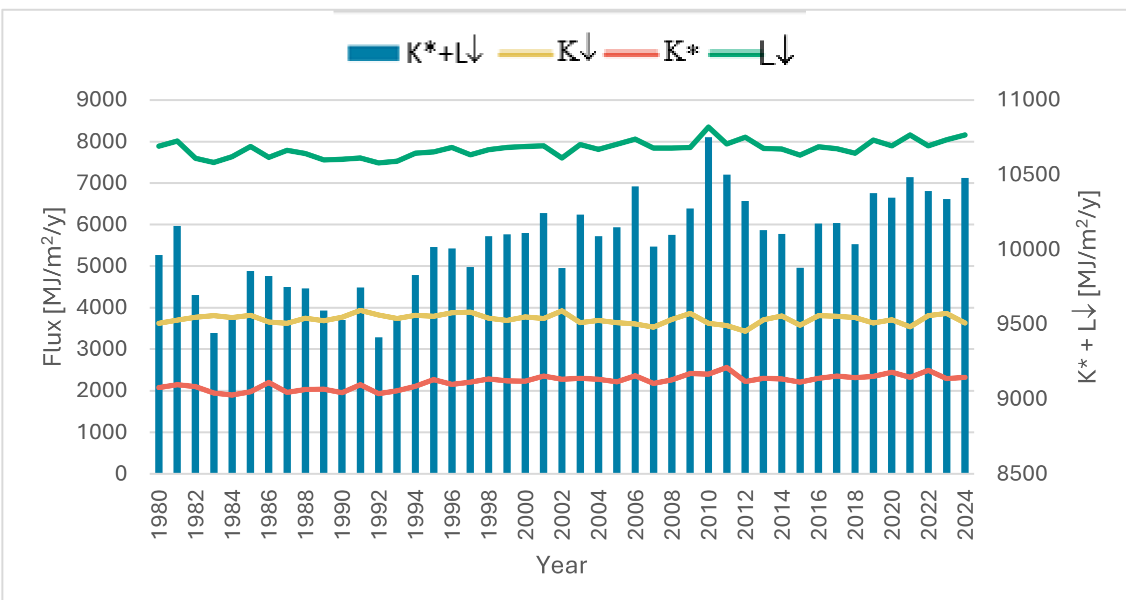

Figure 14d - Radiative forcing components of JB from 1980 to. 2024 ($p<0.001$). Insolation (K↓) is shown for reference

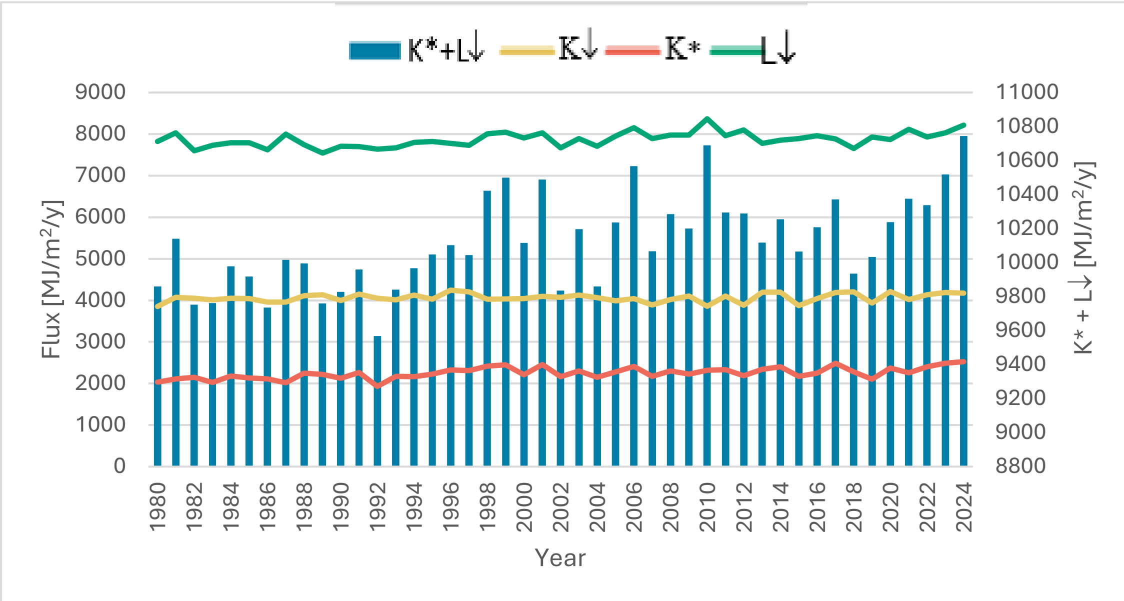

Figure 14e - Radiative forcing components of HBC from 1980 to 2024 ($p<0.001$). Insolation (K↓) is shown for reference

The relationship between radiative forcing and thermal response is shown in Figure 19. Annual surface temperature is tightly regulated by the combined inputs of longwave and absorbed shortwave radiation in all sub-basins ($p < 0.001$). Year to year variability in temperature is best accounted for in Hudson Strait and Foxe Basin ($R^2 > 0.95$) and poorest in James Bay ($p > 0.86$) with 93% of the variability in temperature accounted for by the variability in radiative forcing in HBC as a whole.

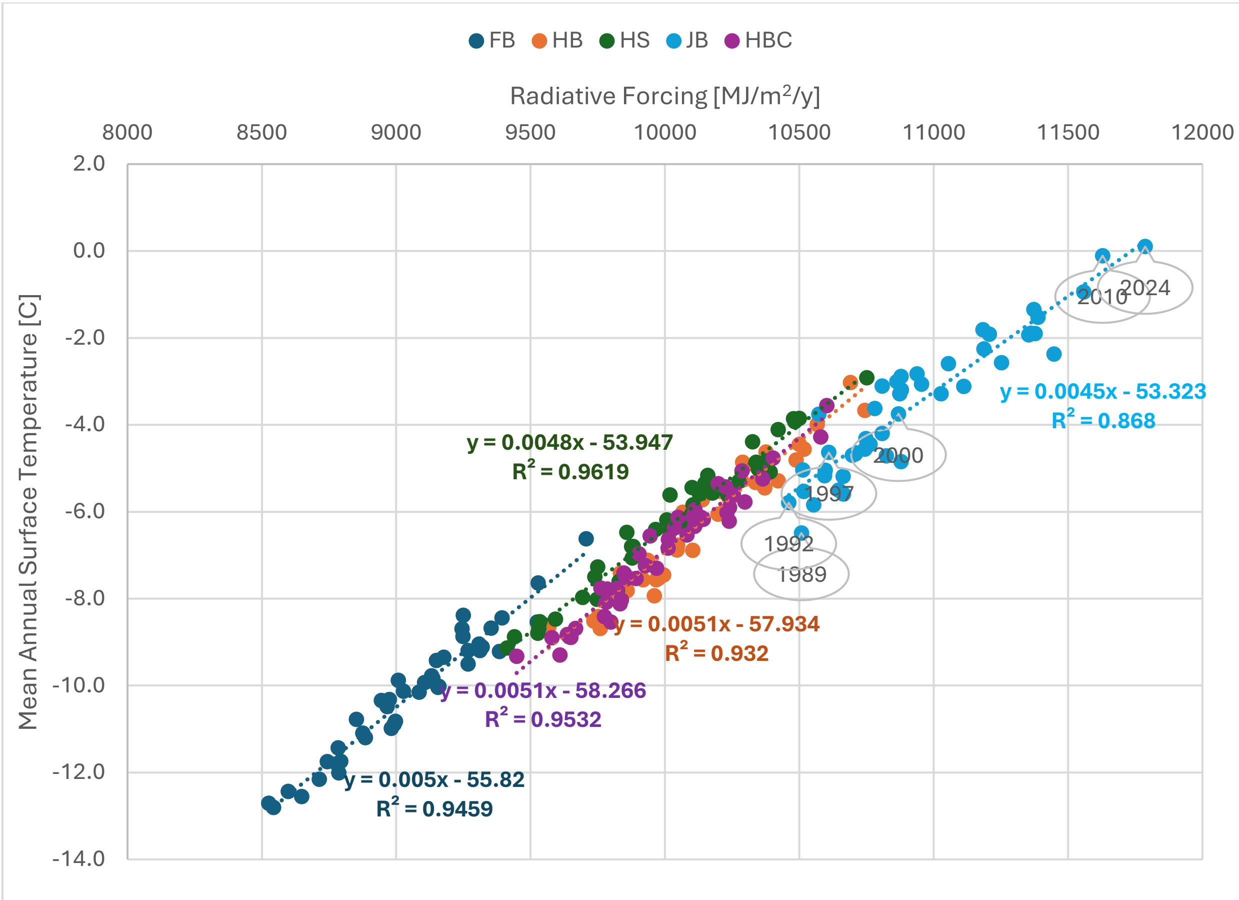

Figure 15 - Relationship between annual surface temperature and radiative forcing.

4.6 Convection

Annual latent and sensible heat fluxes exhibited distinct long-term trends across the five major waterbodies (FB, HB, HS, JB, and HBC) between 1980 and 2024 (Figures 16–17). Losses of latent heat showed significant enhancements in four of the five systems (Figure 16). FB demonstrated the weakest loss of latent heat with a clear decline ($p < 0.01$), while HS, JB, and HBC all exhibited stronger annual losses that strengthened over time ($p < 0.001$). The magnitude of change varied among regions, with JB and HS showing steeper trends relative to FB and HBC. In contrast, HB displayed no statistically significant trend over the study period. The strength of the regression fits (R^2 values) indicated that variability was more strongly captured in JB and HS, suggesting a more consistent regional pattern of decreasing latent heat flux in these waterbodies compared to HB and HBC.

Patterns in sensible heat flux also revealed declining trajectories, but with greater variability across systems (Figure 17). JB again demonstrated the strongest intensification of sensible heat loss ($p < 0.001$), while FB, HS, and HBC showed significant but weaker changes ($p < 0.05$). HB remained the only system without a significant change in sensible heat flux, reflecting its comparatively small signal to noise ratio. Regression diagnostics showed that James Bay exhibited the smallest inter-annual variability relative to its trend, whereas the other systems, particularly HB, exhibited lower R^2 values. Together, these results demonstrate that latent and sensible heat fluxes are generally strengthening across most of the sub-basins, with the most consistent and significant changes occurring in JB. The lack of significant change in HB suggests regional heterogeneity in energy exchange processes, with HB remaining comparatively resistant to the broader trends observed elsewhere.

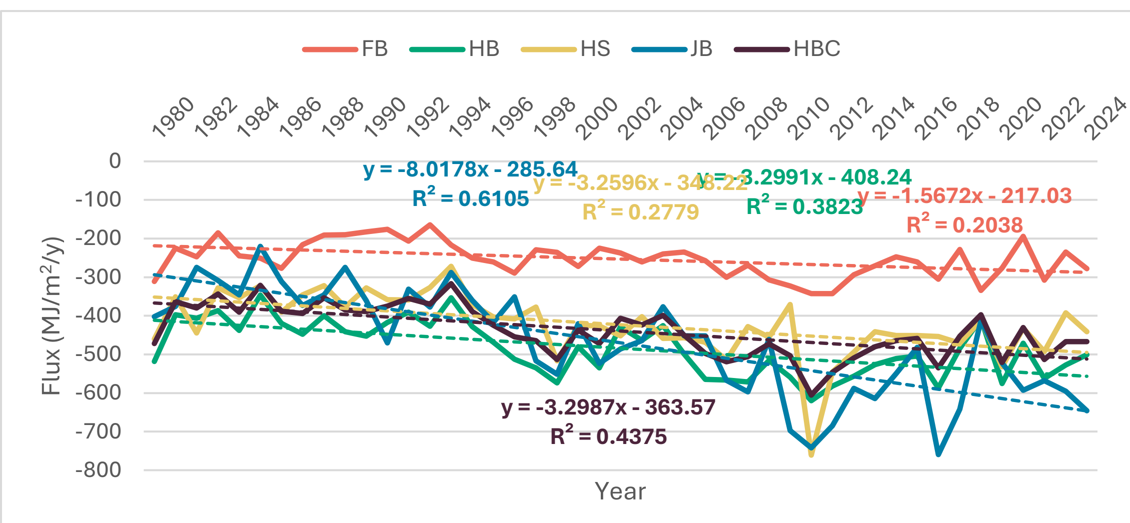

Figure 16 - Annual latent heat flux (MJ/m2/y) from 1980 to 2024 across the five waterbodies (FB, HB, HS, JB, and HBC). FB is significant at $p < 0.01$, the others are significant at $p < 0.001$.

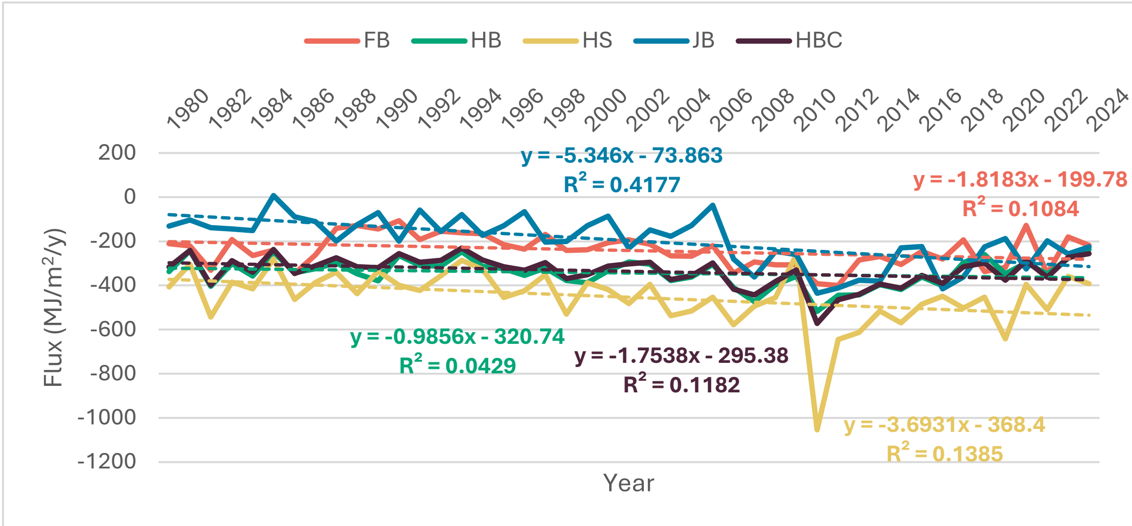

Figure 17 - Annual sensible heat flux (MJ/m^2/y) from 1980 to 2024 across all sub-basins and HBC). HB is not significant, FB, HS, and HBC are significant at $p < 0.05$, while JB is significant at $p < 0.001$.

4.6 Net Surface Energy Exchange

4.6.1 Long-Term Patterns in Qs

The patterns of annual surface energy exchange are shown in Figure 18. JB stands out as a location where surplus energy is being accumulated at the surface each year averaging 680 ± 233 MJ/m^2/y over the study period. It does display a statistically significant ($p < 0.001$) declining trend although superimposed on this is large interannual variability with the suggestion of subsets of years undergoing decline and then recovery. At the other extreme is FB which shows a 45-year deficit of surface energy averaging -144 + 114 MJ/m^2/y and no statistically significant linear trend. HB and HS also show no significant linear trends with long-term averages of 63 ± 141 and -78 ± 208 MJ/m^2/y, respectively.

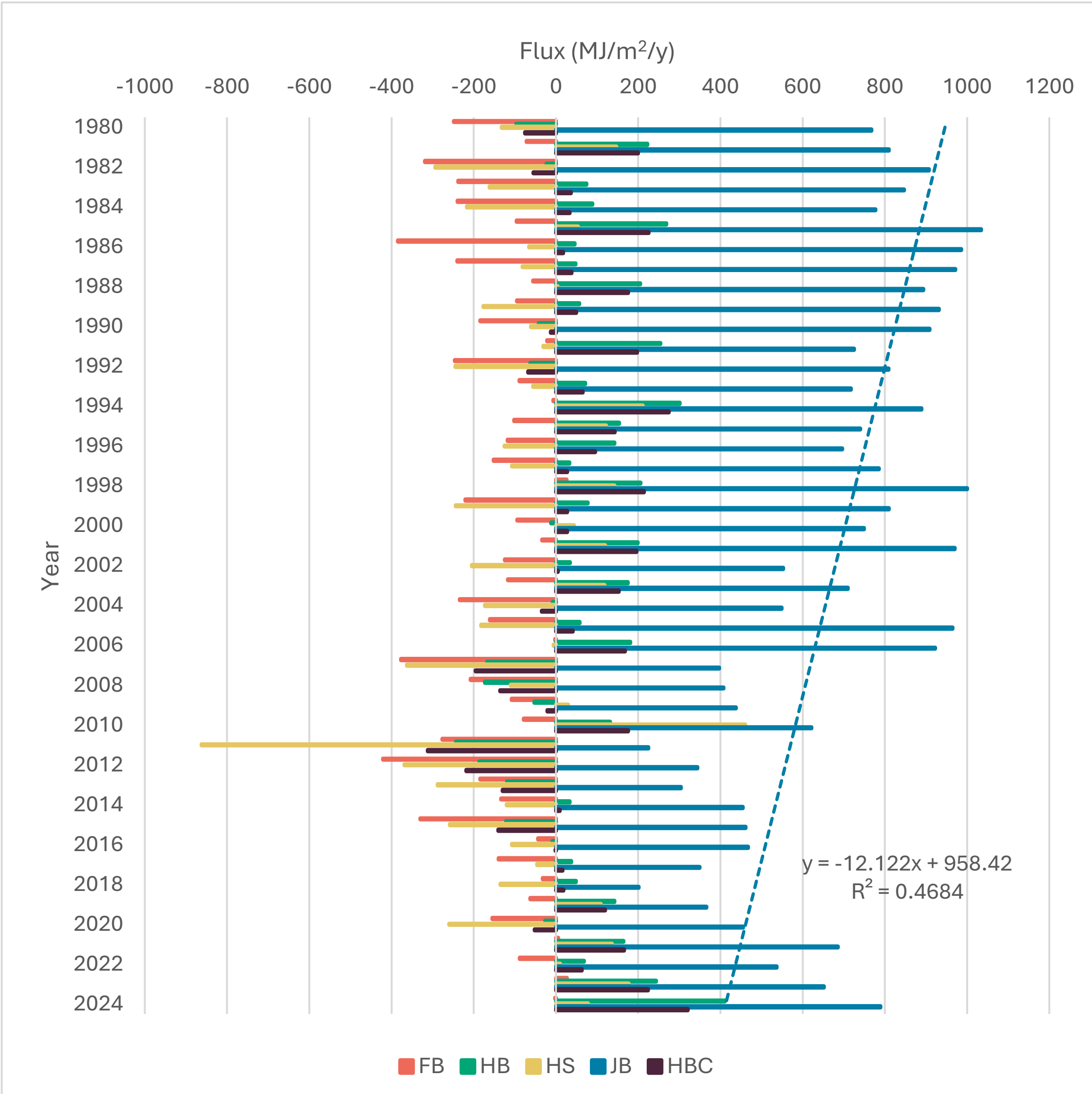

Figure 98 - Annual subsurface heat flux (MJ/m²/y) from 1980 to 2024 across each sub-basin. Any linear trends in FB, HS, and HB are statistically insignificant; JB is decreasing significantly at $p < 0.001$.

While all sub-basins suggest an increasing annual surplus (or decreasing deficit) over the most recent decade, only Hudson Bay registers 2024 as a maximum. As a whole, the HBC shows no linear trend in Qs and shows an average surplus of 46 ± 135 MJ/m²/y. For later reference, the HBS excluding HS, shows a larger 45-year mean surplus of 67 ± 130 MJ/m²/y without a trend (not shown).

4.6.2 Factors Contributing to Variations in Qs

Figures 19a-e show the component fluxes making up annual energy exchange over the study period. Surface energy budgets indicated strong sub-basin variability, as basin-wide differences in net radiation (Q*), latent heat (Q_E), and sensible heat (Q_H) dominated the observed shifts. In all sub-basins, convection and net radiation accounted for some of the largest components of surface energy exchange, with net radiant gains averaging 423 ± 111, 967 ± 100, 898 ± 129 and 1224 ± 152 $MJ/m^2/y$ for FB, HB, HS and JB, respectively. Corresponding convective losses average -481 ± 113, -828 ± 120, -877 ± 207 and -667 ± 203 $MJ/m^2/y$. For HBC, net radiant gains of 900 ± 95 $MJ/m^2/y$ are offset by -775 ± 123 $MJ/m^2/y$ of convective losses yielding a net annual surplus of 125 $MJ/m^2/y$ due to these two factors alone.

The impact of latent energy extraction of surface energy from melting snow, Q_{Lf}, shows no trend over the study period in any of the sub-basins with very little interannual variability (Figures 19a-e). This is consistent with the values for annual snowfall, shown in Figure 4c. The mean net Q_{Lf} flux of -79.5 ± 5.87 $MJ/m^2/y$ for HBC over the study period represents the difference between the gross snowfall flux of -80.9 ± 5.9 $MJ/m^2/y$ minus loss of mass arising from annual snow evaporation of 1.2 ± 0.15 $MJ/m^2/y$. Sensible energy transfer from precipitation to the ocean surface, Q_P is very small on an annual basis averaging 0.25 ± 0.81 $MJ/m^2/y$ over the study period. Overall, the positive value suggests that annually, falling precipitation is marginally warmer than the underlying surface on average. Although included in the annual estimates of the surface energy budget, Q_P is not shown here. The inclusion of the sensible and latent energy transfer at the surface by precipitation reduces Q_S for the Hudson Bay Complex to an annual surface energy surplus of 46 ± 125 $MJ/m^2/y$ on average between 1980 and 2024. JB exhibited pronounced increases in subsurface (Q_S) and latent heat fluxes, underscoring its sensitivity within the basin (Figures 19a–e).

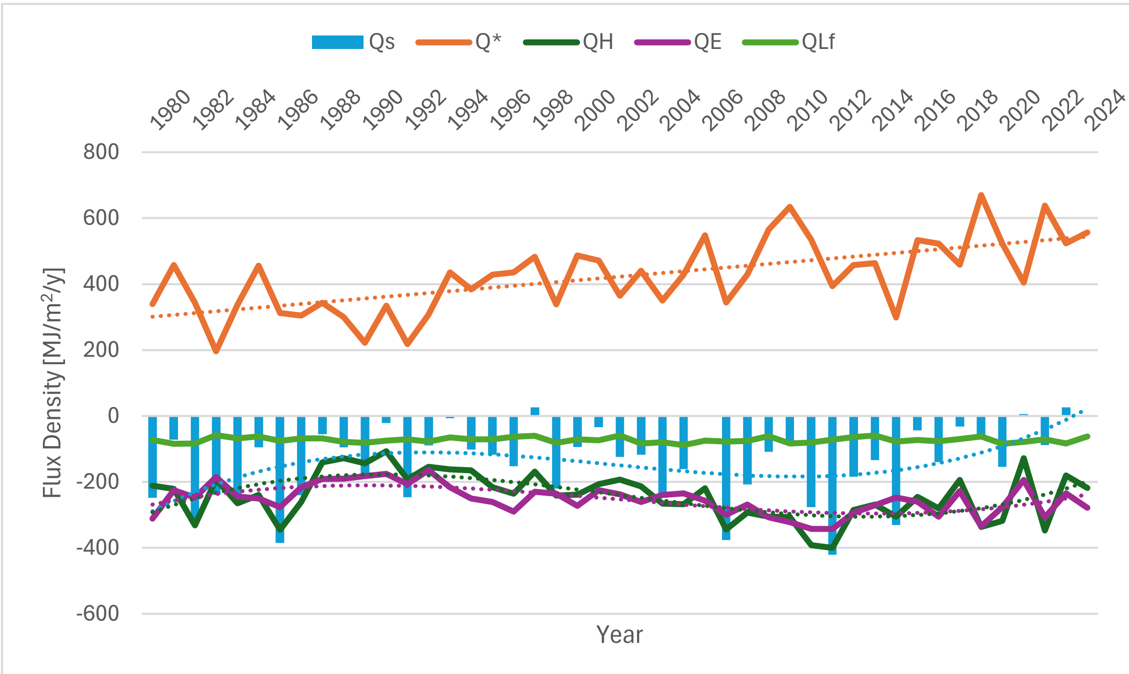

Figure 19a - Annual surface net exchange for FB ($MJ/m^2/y$) from 1980 to 2024.

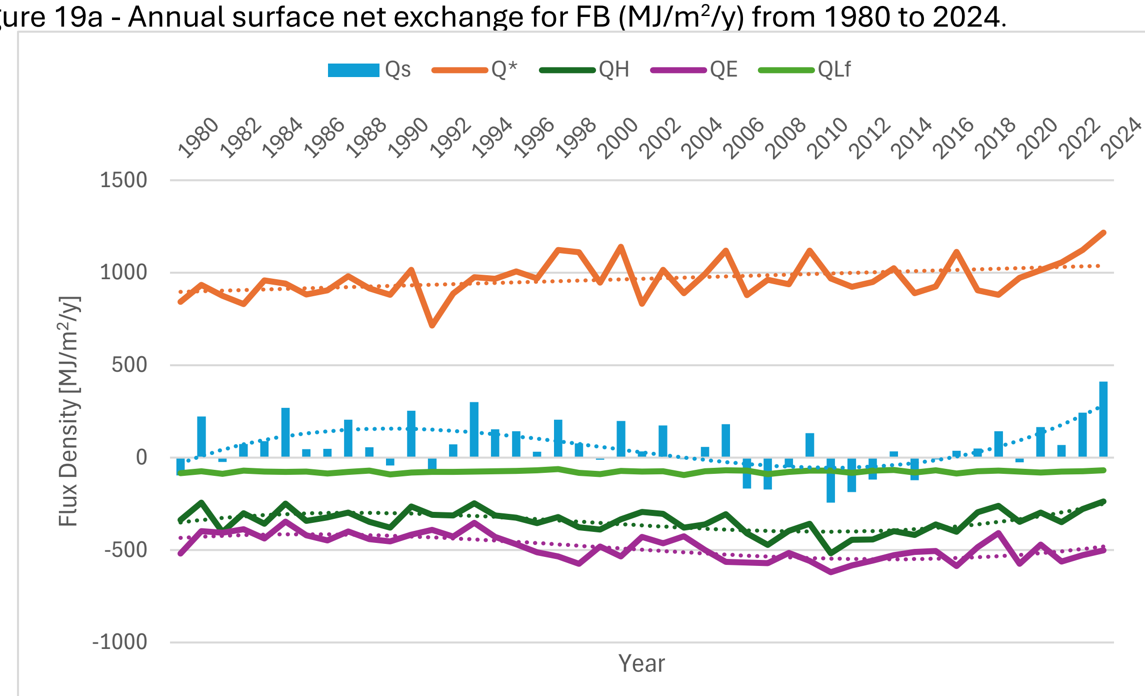

Figure 19b - Annual surface net energy exchange for HB ($MJ/m^2/y$) from 1980 to 2024.

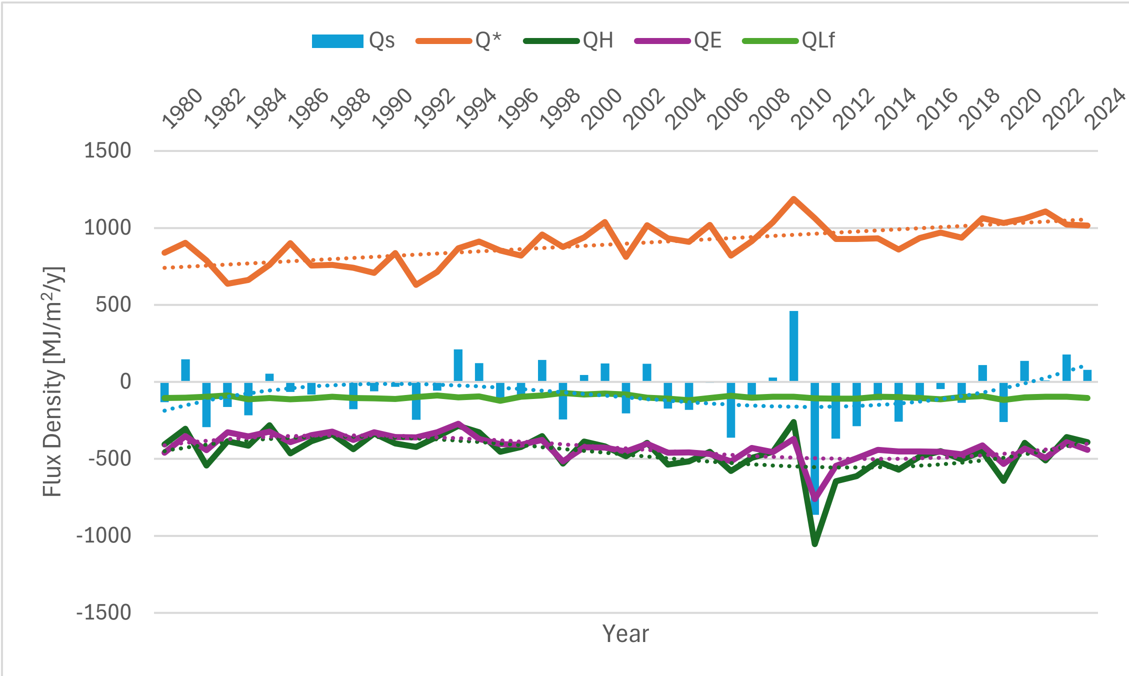

Figure 19c - Annual surface net energy exchange for the HS (MJ/m^2/y) from 1980 to 2024.

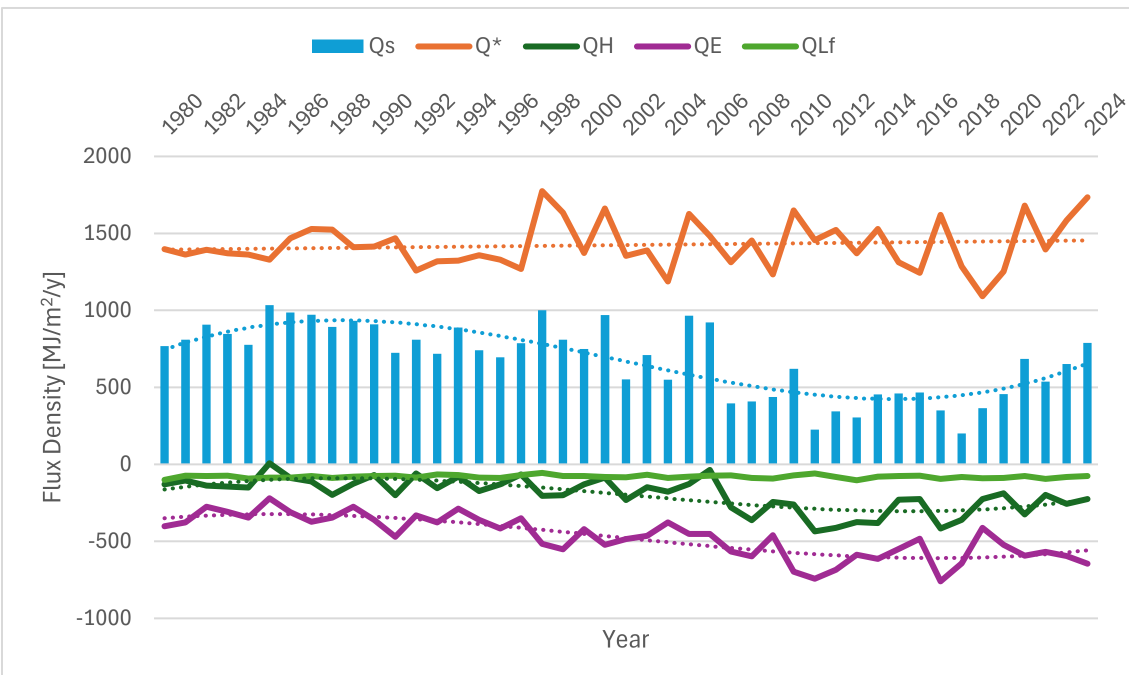

Figure 19d - Annual surface net energy exchange for the JB (MJ/m^2/y) from 1980 to 2024.

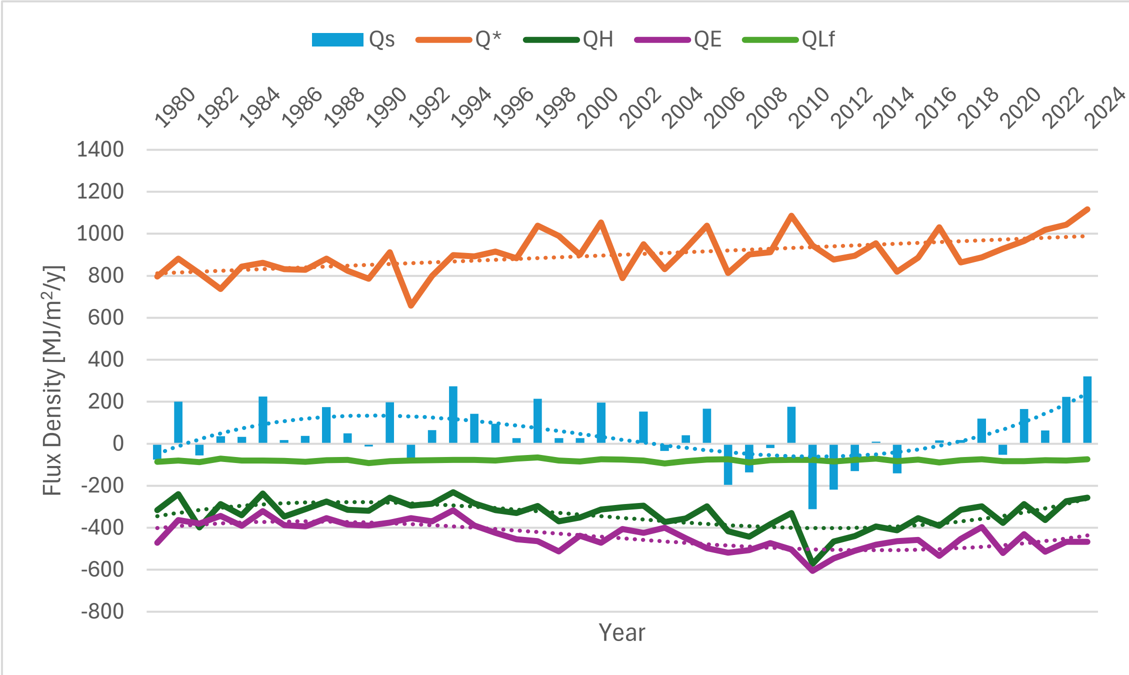

Figure 19e - Annual surface net energy exchange for the HBC ($MJ/m^2/y$) from 1980 to 2024.

The patterns in Qs over the study period are clearly non-linear, despite the observation that a number of other factors vary linearly, often in a highly significant manner. In Figures 19a-e, a 3rd order polynomial has been fitted to the Qs data, not because there is any inherent physical reason this function should provide a best-fit for this 45-year pattern, but because the coefficients of determination for this non-linear function typically exceed $R^2 > 0.5$, far exceeding the linear R^2 coefficients (i.e. the variability in the dependent variable is better explained as a non-linear function of time). The 45-year patterns in Q_H, Q_E and $Q_H + Q_E$ also exhibit the same pattern as does the annual vertical temperature gradient (T_0 - T_2) shown in Figure 6ab. The vertical temperature gradient directly drives the sensible heat flux and to a lesser extent the latent heat flux, so this agreement is not unexpected. What is unclear is the extent to which these undulations in convection are driven by local or external factors.

Figure 20 compares the coupling between the sensible and latent heat fluxes over 45 years to their respective vertical gradients in temperature and vapor pressure. [Vapor pressure gradients were not available from ERA5 and are approximated here using the annual Bowen Ratios, $\beta = \gamma\Delta T/\Delta e = Q_H/Q_E$, where γ = 0.066 kPa/°C is the psychrometric constant (Appendix Table A).]

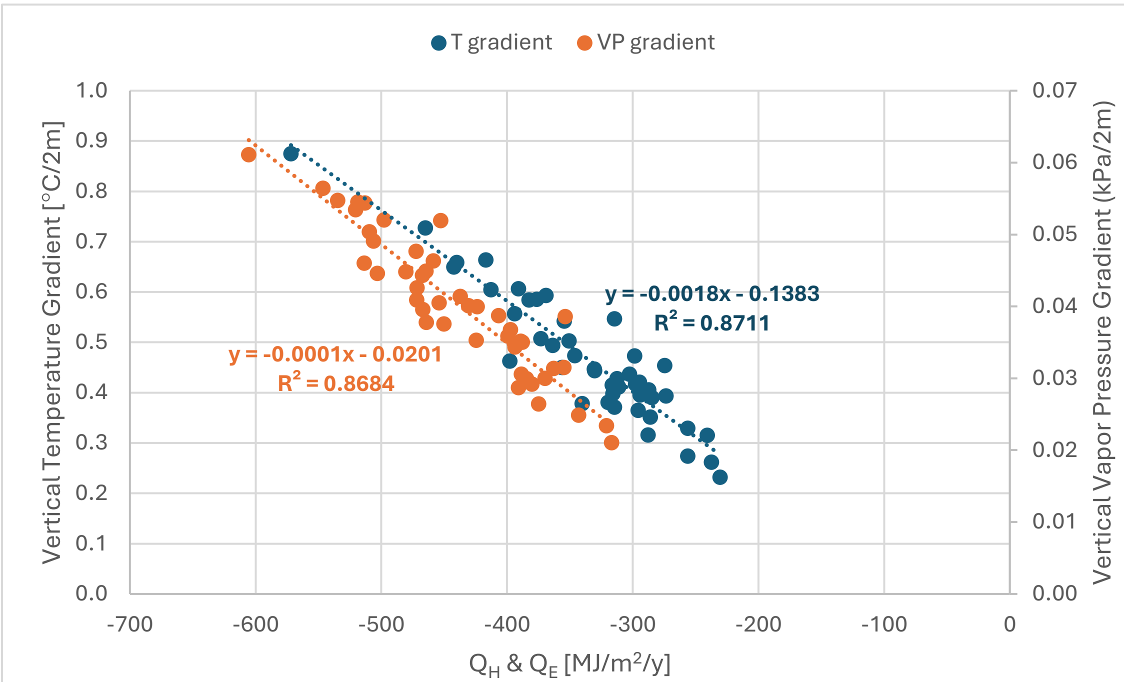

Figure 20 - Relationship between annual Q_H and Q_E fluxes and their respective annual vertical gradients in temperature and vapor pressure for the Hudson Bay Complex.

As expected, the convective fluxes and their respective vertical gradients are highly correlated. Scatter in the relationships is like likely due to interannual variations in the turbulent transfer coefficients, whereby years with higher winds would generally experience stronger fluxes for the same gradient and vice versa. [ERA5 turbulent transfer coefficients were not available for download and ERA5 windspeeds were not downloaded.] Figure 21 shows the annual approximations for the turbulent transfer coefficients for sensible heat at standard atmospheric pressure, where the aerodynamic resistance, $r_a = \rho c_p (\Delta T/\Delta z)/Q_H$.

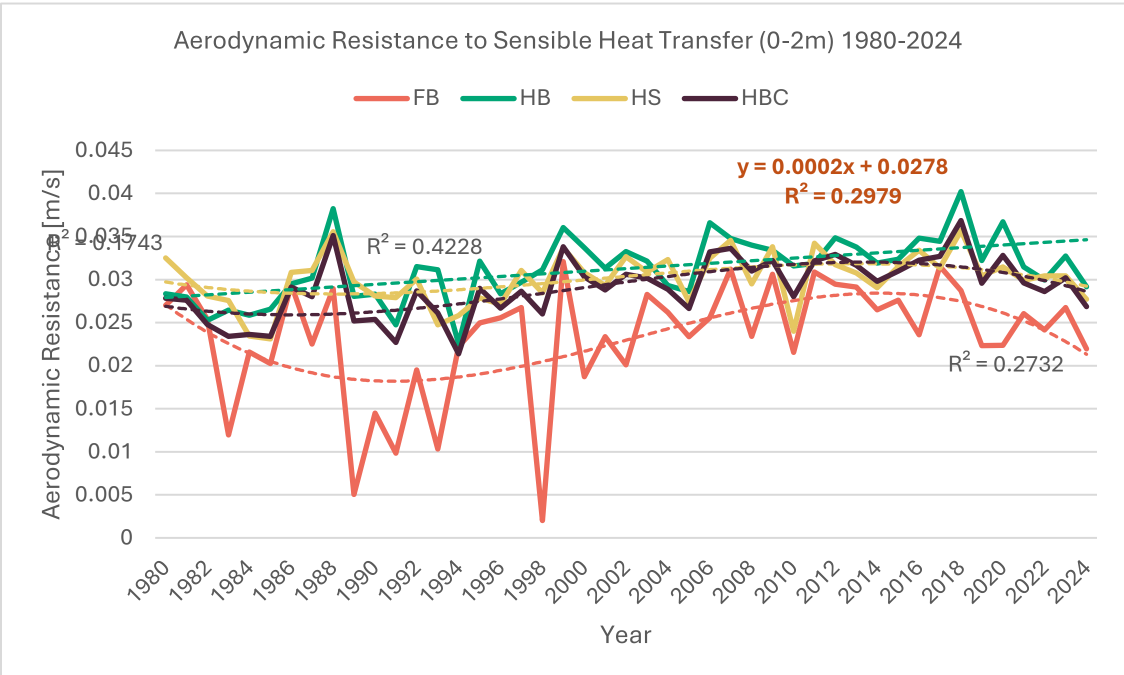

Figure 21 - Derived values of the aerodynamic resistance between the surface and 2m from annual model values of the sensible heat flux and vertical temperature gradient. Dry air density is assumed at the mean layer temperature at standard atmospheric pressure.

The aerodynamic resistance between the surface and 2m appears to increase slightly over the study period. However, it is only HB which has a statistically significant trend ($p < 0.01$), in part owing to the very large interannual variability in ra especially for Foxe Basin. The inverse relationship between aerodynamic resistance and windspeed indicates that over the study period, FB consistently experiences higher windspeeds than the other sub-basins ($p<0.001$) with exceptionally windy conditions during the 1990's. However, this simple explanation may also be influenced by changing seasonality in ice conditions over the study period impacting the annual fluxes and surface roughness which is beyond the scope of this thesis. Nevertheless, with a few exceptions, changes in the annual vertical gradients represent a valid explanation for interannual variations in convective loss of energy from the sea surface.

Figure 22 plots the residuals (Y-Y') between the ERA5 measured (Y) and estimated (Y') surface temperatures from the radiative forcing regressions shown in Figure 15. Although the residuals are small, it is clear that there is a non-linear component to the increase in ERA5 surface temperatures over time which is not captured by the linear increase in radiative forcing. These coincide with the non-linear undulations in the vertical temperature gradient (Figure 9b). The coincidence does not necessarily establish cause and effect although surface warming is more closely tied to radiation absorption at the surface, than it would influence the air temperature at 2m above the surface.

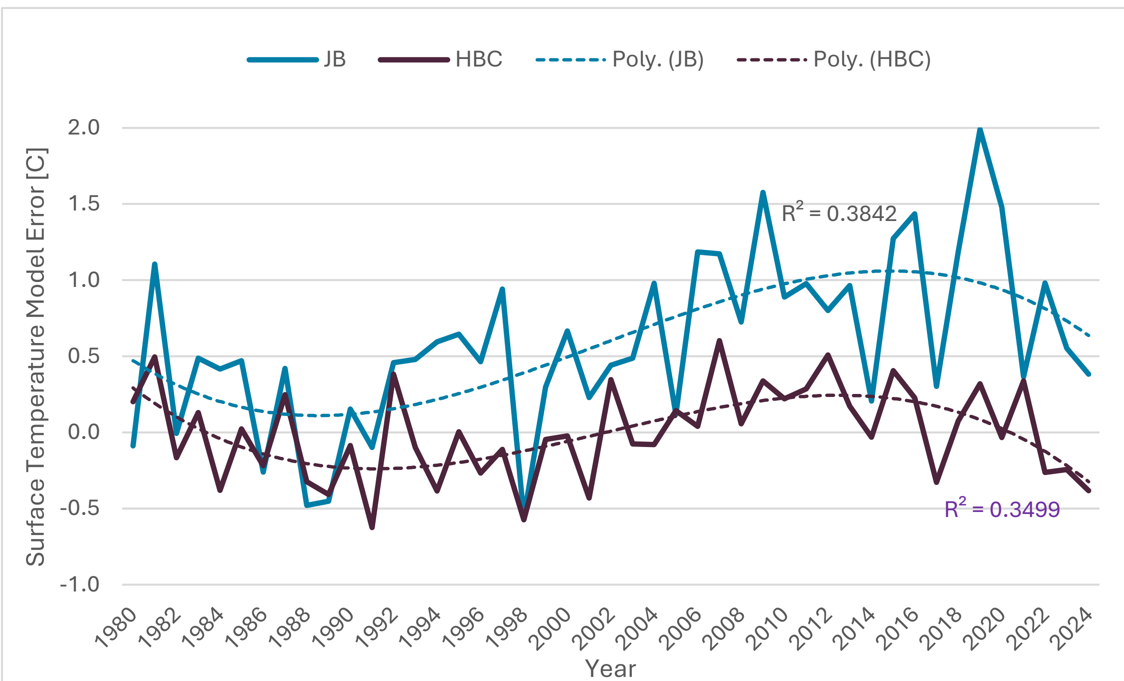

Figure 22 - Residual temperature errors (T-T') for the Hudson Bay Complex and James Bay from radiative forcing regressions of T'_0 and ERA5 T_0 over the study period.

4.6.3 Impacts of Variations in Qs

I now address the impacts of variations in annual Qs. The annual surpluses and deficits from the surface energy balance can either be accommodated by annual changes in energy storage and/or annual transport across the boundaries of the system. For sub-basins like JB which shows a consistent annual surplus it is physically realistic to expect a net energy export to HB with which it shares a boundary, and which has a much smaller surplus. Conversely, Foxe Basin with a persistent energy deficit might be expected to consistently gain energy from HB or HS with which it shares boundaries which exhibit energy surpluses. As a whole, the HBC would primarily export or import energy with the Labrador Sea. To get a sense of the magnitude of this horizontal marine transfer we might first account for the non-steady state conditions within the water column in order to estimate the magnitude of potential net advective transport as a residual. The increases in annual average surface temperature are the only direct observational evidence available that steady-state conditions do not exist. ERA5 does provide an estimate of the temperature of the surface layer of the ocean (SST) between 4 and10 m which is intended to provide a *foundation* daily temperature that is free from daily variations due to the diurnal cycle of the sun (Yang et al. 2022).

In what follows, I first hypothesize that over 45 years, the water column of the HBC has responded homogenously to the mean surface energy surplus of 46 MJ/m^2/y. This implies that $\Delta T/\Delta t$ is invariant with depth. Applying this constraint to the mean water depth of 115 m for HBC (Table 2) yields an average thermal response of 0.0955 °C/y. The observed surface temperature increases more slowly at 0.0751 °C/y. This discrepancy could be reconciled if (1) the annual mixed layer extends to a depth of 146 m instead of 115 m, (2) the annual component of surplus energy going into energy storage is 36 MJ/m^2/y (78.6% of 46) or alternatively (3) that 21.4% is going into ice-melt, equivalent to -33 mm SWE per year. The first possibility is unlikely implying an error in model bathymetry. The second outcome is plausible but untestable without time series temperature estimates in the water column. The third outcome is plausible but without an independent estimate of the rate of ice-melt, is not directly testable. However, given some published estimates of HBC ice thickness averaging ~1.6 m (England et al. 2025), this would imply complete ice disappearance in 48 years. This is a very rapid decline in sea-ice cover compared to the 221 years suggested by the linear extrapolation of SIC decline for HBC from Figure 8.

An alternate hypothesis is that the actual long-term warming rate is provided by the long-term observed rate of increase in surface temperature provided by linear regression. Implicit in this hypothesis is the assumption that all gains in energy are sensible and involve no reduction in mean ice thickness and that the annual warming rate is homogenous throughout the water column. Applying the warming rate of 0.0751 °C/y yields a change in energy storage of 36 MJ/m^2/y as outlined earlier. My intention is to use this as a baseline to normalize the required net energy export or import to achieve an energy balance of zero, annually. Before proceeding, we will apply the two hypotheses to the Hudson Bay System conceptual framework by excluding Hudson Strait and considering it a conduit for energy and mass transfer with the Labrador Sea. The observed surface warming rate for HBS is 0.0743 °C/y from regression and represents a warming rate consistent with the long-term average Qs of 67 MJ/m^2/y for a mean HBS depth of 106 m. This yields an equivalent thermal response of 0.115 °C/y. This second framework also supports the conclusion that the 45-year mean Qs is a poor assumption for annual energy storage without unrealistic reductions in ice-thickness. For HBS, the surface-temperature-derived annual change in storage is 33 $MJ/m^2/y$. This is 92% of the corresponding mean change in storage for HBC and 49.2% of the long-term surface energy balance for HBS of 67 $MJ/m^2/y$. The actual non-steady-state rate of increase in energy storage remains unresolved.

The annual energy balances for HBC and HBS normalized to their respective 45-yr means are shown in Figure 23. In general, in years with a surplus of energy implying net export ($Qs > 0$) the energy leaving HBS exceeds the energy leaving HBC ($Qs_{HBS} > Qs_{HBC}$) This implies more energy is entering Hudson Strait by exiting the interior sub-basins than is exiting Hudson Strait to the Labrador Sea and therefore HS is serving as a net energy sink ($Qs_{HBC} - Qs_{HBS} = \Delta Qs < 0$). In general, during years with a deficit of energy, implying net import ($Qs<0$), HBC is importing more energy than is being imported by HBS implying that Hudson Strait is again serving as an energy sink ($\Delta Qs < 0$). However, there are three exceptions in which $\Delta Qs > 0$ and these are consecutive years 2008, 2009 and 2010 when

Hudson Strait is acting as an energy source of ΔQs = 4.5, 8.7 and 48.7 MJ/m^2/y, respectively (Figure 23).

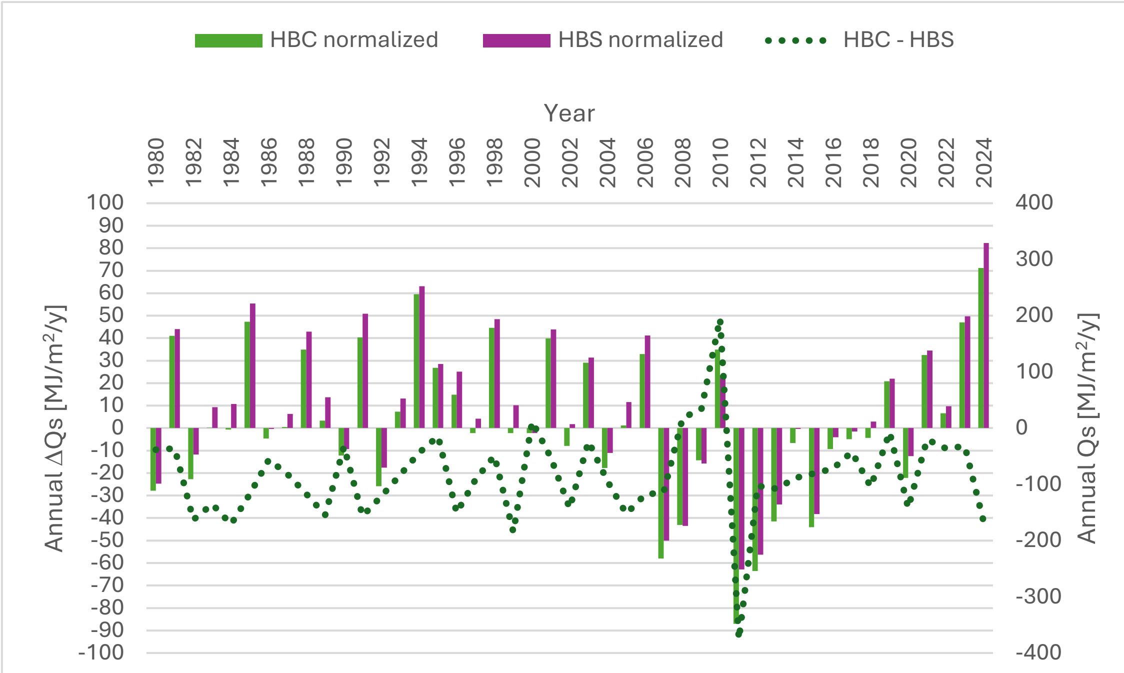

Figure 23 - Pattern is surplus (+) and deficit (-) surface energy budgets for HBC and HBS. $Qs_{HBC} - Qs_{HBS} = \Delta Qs$.

If HS was acting as a passive pipe, it would mean that ΔQs = 0. The fact ΔQs is typically negative suggests that HS is withdrawing energy which appears consistent with it possessing a long-term annual deficit Qs flux of -78 ± 208 MJ/m^2/y. For the three years of 2008 through 2010, the surface energy budget for HS was Qs = -100, 29 and 461 MJ/m^2/y, respectively.

In the interpretation which follows the assumption is made that there is a net annual export of water out through HS to the Labrador Sea. This is supported by previous research which estimates that freshwater discharge flowing into the HBC system from major rivers is equivalent to approximately 64 ± 4 cm per year (Dery et al. 2005). Conservation of mass requires annual freshwater inputs to balance brackish water outputs provided there is near balance between annual precipitation and evaporation. However, this analysis indicates that there exists a precipitation excess of 33 ± 3.7, 32 ± 4.0 and 39.2 ± 5.0 cm/y for HBC, HBS and HS, respectively. Therefore, the net annual flow out of HBC is closer to 93 ± 7.7 cm/y approximately 55% larger than river discharge alone and the energy contained in this flow will be exported and not require counterflow to retain mean sea level.

However, energy exchange through Hudson Strait is also driven by dynamical effects primarily associated with semi-diurnal tidal, density and wind driven influences during which higher-salinity and denser water enters through HS, along the northern shore adjoining Baffin Island and less dense, warmer and less saline water exits in a generally shallower current along the southern shore adjoining Quebec (Ridenour et al. 2021). However, there is ample evidence now that some freshwater is also entering HS from southward flowing Baffin Island Current (Ridenour, 2021) which considerably complicates attempts to reconcile the freshwater balance of HBS. Although a temperature gradient likely exists along HS which is seasonally dependent and varies annually, the interannual variability in energy flow entering or leaving HBS due to dynamical influences cannot be estimated using this analysis. Nevertheless, because the effects of tidal mass flow are largely dependent on astronomical factors, it may be that interannual variation is conservative over the study period.

Although my HBS conceptual framework assigns all advective energy exchange through Hudson Strait, there are small mass flows into Foxe Basin via Fury and Hecla Strait. And river discharge is transporting energy into the HBS across the boundaries of the HBS domain. There are some studies estimating the thermal impacts of this flow for rivers but only on the west side of Hudson Bay. With the approximation that roughly 50% of the annual surplus of 67 MJ/m^2/y from HBS goes into an increase in energy storage, the remaining half is exported annually on average over the study period. This long-term net advection of -34 MJ/m^2/y is 41% of the energy loss due to snow melt (Q_{Lf})or equivalent to 9% of the annual radiant gains. Although this advective loss is relatively minor, its interannual variability is extremely large and could be responsible for the interannual variability in the timing and duration of the ice seasons (Figure 7a-e) and therefore requires further analysis.

4.7 Spatial Changes in Q_S for Select Years.

Figures 24a–e shows the temporal distribution of the modeled surface energy surpluses and deficits across the Hudson Bay watershed for the years 1980, 1987, 2005, 2011, and 2024. These years were chosen to illustrate the beginning and end years of the study period (1980 and 2024); as well as the most "neutral" or "extreme" years. Across all years, values exhibit a pronounced latitudinal gradient, with the highest annual surpluses concentrated in the southern portions of James Bay and progressively weaker surpluses and stronger deficits extending northward into Foxe Basin. In 1980 at the start of the study period (Figure 24a), most of the HBC was characterized by low values (light green), particularly across the northern and coastal regions, specifically FB. High-intensity values were confined to JB, with the maximum class (dark red) occurring in a localized area adjacent. By 1987 (Figure 24b), intermediate value classes (orange-yellow) expanded northward into central portions of the watershed, mainly central HB, replacing areas that had previously belonged to lower classes. The highest class (dark red) remained localized in the southern margin near JB but increased in spatial extent compared with 1980.

In 2005 (Figure 24c), the south–north intensification became more pronounced. The mid-range class (green-yellow) spread further northward across central Hudson Bay, while values in the class (red-orange) began to dominate large portions of the southern basin. The highest class expanded across a broader area, suggesting an intensification of conditions in JB. By 2011 (Figure 24d), much of central HB was dominated by elevated classes (red), while pockets of the highest class extended beyond the southern fringe into mid-latitude regions of the watershed. Lower classes (blue) were increasingly restricted to the far northern FB and coastal margins.

The 2024 distribution at the end of the study period (Figure 24e) demonstrates the most extensive intensification. High-value classes (orange-red) dominated JB through central HB, while the maximum class (dark red) covered a large, nearly continuous swath extending from the southern boundary well into the mid-latitude watershed. In contrast, low-value classes were limited almost exclusively to FB's coastal areas.

Overall, the results indicate a progressive intensification and northward expansion of energy budget surpluses within the HBC between 1980 and 2024. Grid cells in the highest class increased steadily over the study period, transforming from sparse and localized in 1980 to widespread and dominant by 2024. Simultaneously, lower-value classes retreated toward the northern and coastal margins, underscoring a large-scale redistribution of the annual energy balance across the basin.

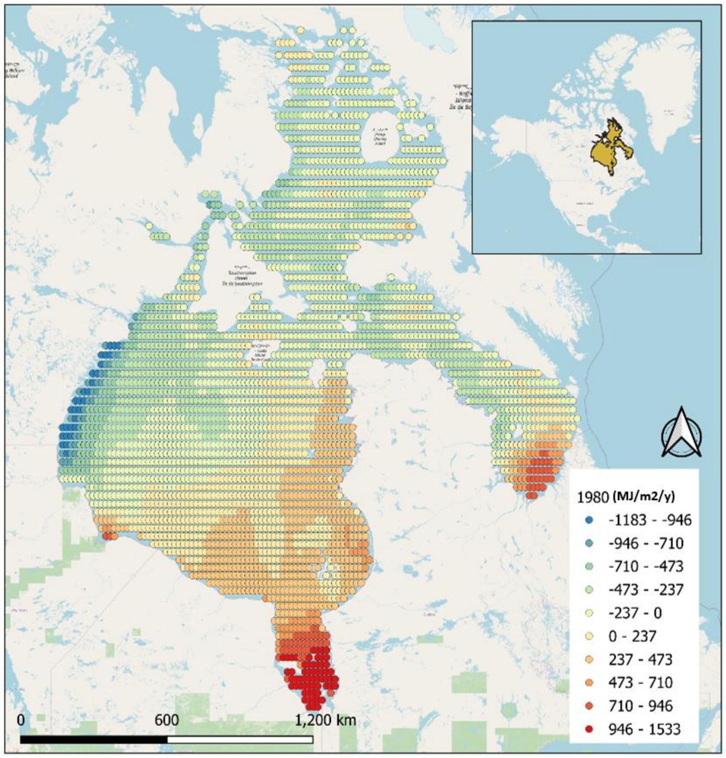

Figure 24a - Spatial distribution of annual subsurface heat flux (Qs = -76 MJ/m^2/y) across the HBC for the year 1980. Annual deficits (cooling) are displayed in shades of blue/green. Annual surpluses (warming) are displayed in shades of orange/red.

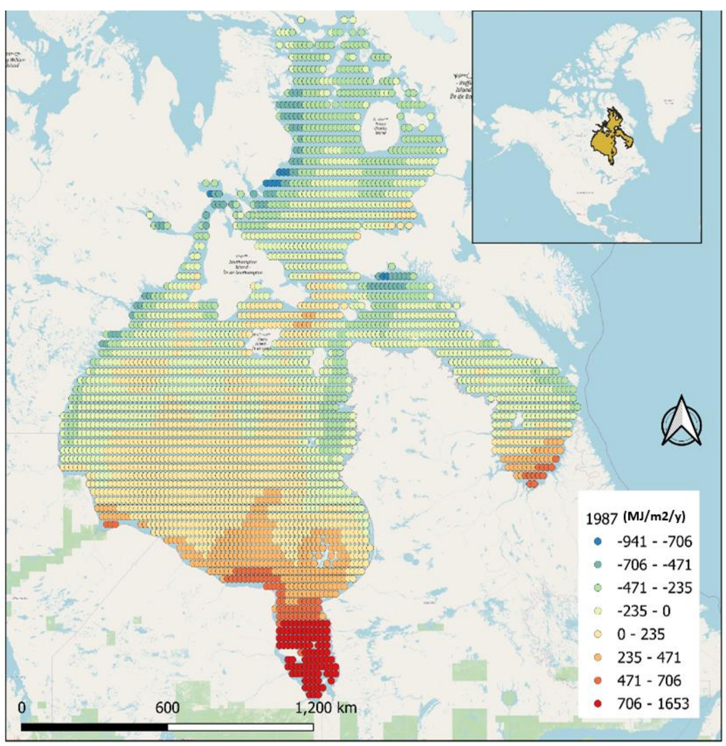

Figure 24b - Spatial distribution of annual subsurface heat flux (Qs = 38 MJ/m^2/y) across the HBC for the year 1987. Annual deficits (cooling) are displayed in shades of blue/green. Annual surpluses (warming) are displayed in shades of orange/red.

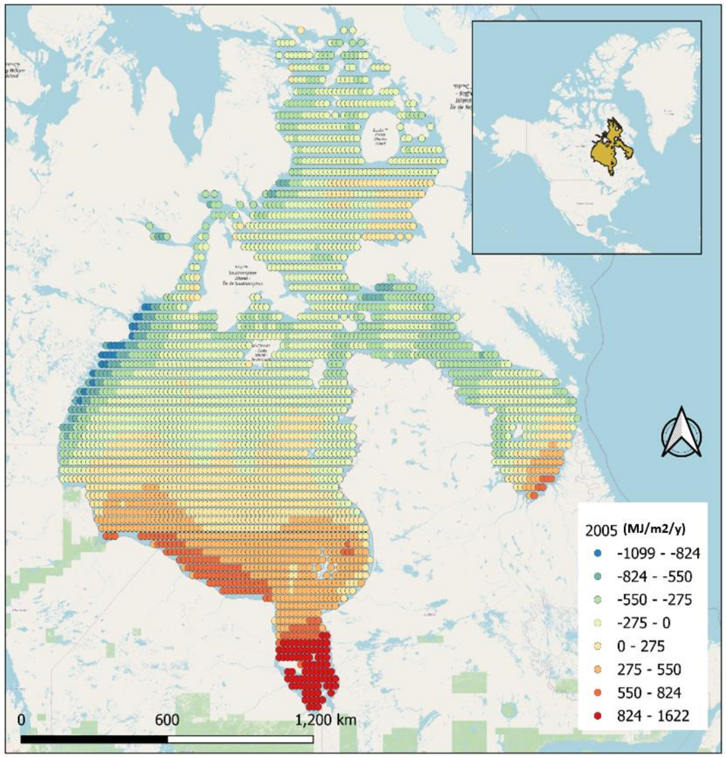

Figure 24c - Spatial distribution of annual subsurface heat flux (Qs = 41 MJ/m²/y) across the HBC for the year 2005. Annual deficits (cooling) are displayed in shades of blue/green. Annual surpluses (warming) are displayed in shades of orange/red.

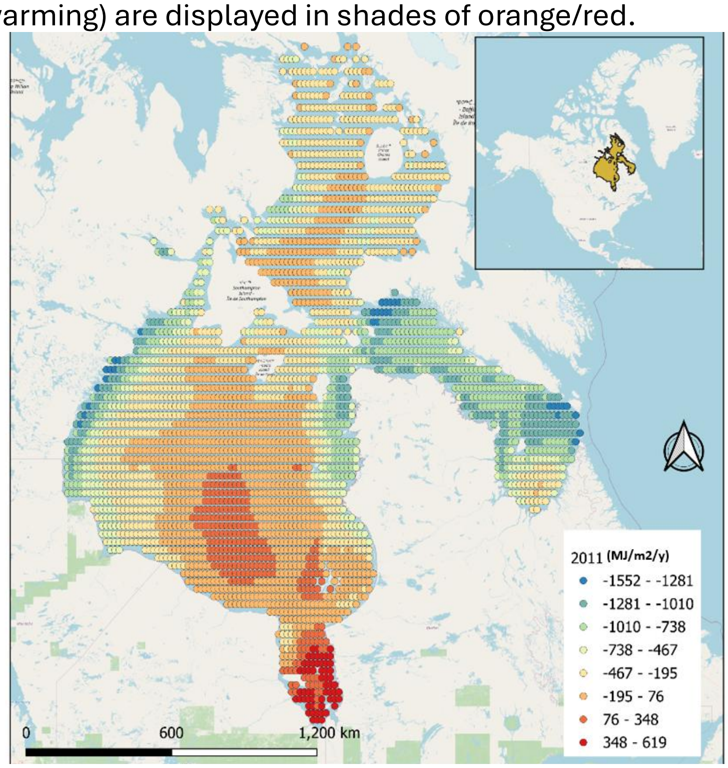

Figure 24d - Spatial distribution of mean annual subsurface heat flux (Qs = -312 MJ/m²/y) across the HBC for the year 2011. Annual deficits (cooling) are displayed in shades of blue/green. Annual surpluses (warming) are displayed in shades of orange/red.

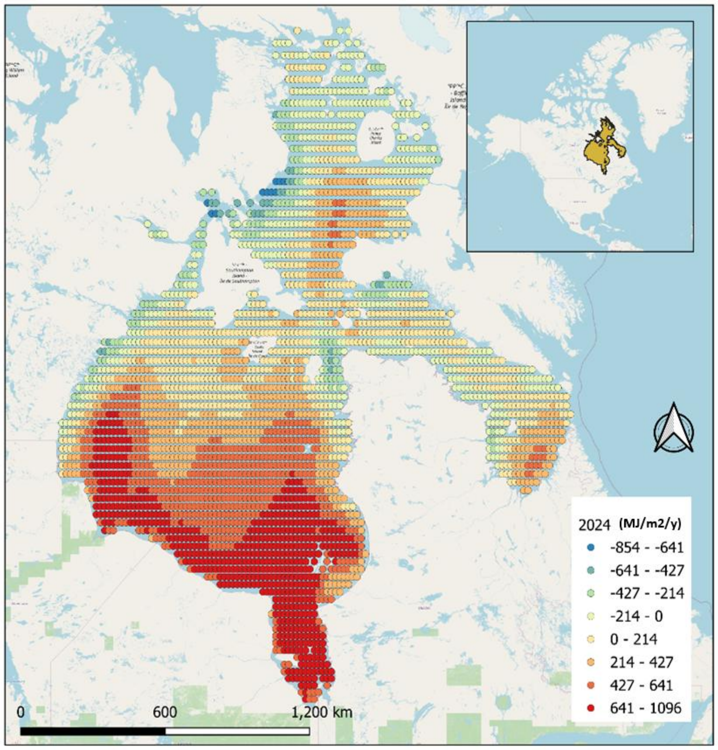

Figure 24e - Spatial distribution of annual subsurface heat flux (Qs = 321 MJ/m^2/y) across the HBC for the year 2024. Annual surpluses (cooling) are displayed in shades of blue/green. Annual deficits (warming) are displayed in shades of orange/red.

Chapter 5 – Discussion

5.1 Key Findings

This study provides the first comprehensive thermodynamic audit of the Hudson Bay Complex (HBC) using ERA5 reanalysis from 1980–2024. Several major findings emerge. First, there is strong evidence of intensified radiative forcing driven primarily by the ice–albedo feedback, with net shortwave absorption increasing significantly despite no long-term change in incoming solar radiation (Hochheim & Barber, 2010; Bello & Higuchi, 2019). Secondly, the greenhouse effects driving changes in L↓ are virtually the same magnitude as those of the ice-albedo feedback. The 1992 perturbation in insolation from the eruption of Mt. Pinatubo caused surface temperatures to decrease in 1992 but it was not sufficient to initiate positive ice-albedo feedback to resume ice growth in subsequent years. This is presumably due to the persistent forcing from the greenhouse effect. Achieving net-zero-emissions of greenhouse gases globally could cut the surface warming rate in half potentially but may also increase the sensitivity of surface temperature to albedo changes, perhaps reversing the rate of ice melt following a future volcanic eruption. Both radiant fluxes are dominant drivers of the surface energy balance as 96% of the annual variability in surface temperature is accounted for by the variability in combined radiative forcing over the 45 years of study.

Longwave emissions from the surface offset 91% of the radiative forcing. The remaining net radiation of 900 MJ/m^2/y over the study period is offset by convective losses of 775 MJ/m2/y on average (86%) with the sensible heat flux averaging 77% of the latent heat flux over the study period. But while net radiation has been intensifying linearly over time, the convective fluxes have not; but rather undulate consuming between 61% and 125% of the radiant gains. And because the annual consumption of surface energy by melting snow exhibits modest losses averaging 8% of net radiation without a trend over the study period, the interannual variability in the surface energy balance Qs is mostly driven by the convective losses. Over 45 years, surplus Qs averages 46 MJ/m^2/y but interannual variability ranges from 321 to -312 MJ/m^2/y. If steady state conditions were assumed and all this energy must be advected by current flow through Hudson Strait and Fury and Hecla Strait to maintain a zero balance annually, then 46 MJ/m^2/y is slightly more than half the 80 MJ/m^2/y removed annually by snowmelt over the study period.

There are weak increasing trends in precipitation consistent with modest increases in the hydrologic cycle but no clear trend in net precipitation. Precipitation excess is large exceeding 300 mm per year enhancing the freshwater river discharge inputs to the whole system by 50%. Hudson Strait ranks highest in terms of precipitation excess. These excess inputs of freshwater enhance a net outflow of water out through Hudson Strait which requires no counterflow. Consequently, it represents a mechanism which serves to export surplus energy annually across the boundaries of the system to the Labrador Sea. Hudson Strait along with Foxe Basin are the two sub-basins which represent a long-term surface energy deficit. In the case of Foxe Basin this persistent deficit helps partially offset the long-term surplus in Hudson Bay and extremely large surplus in James Bay.

One major unresolved issue is how the net marine transport through the straits can accommodate the very large swings in surplus or deficit in the surface budget in any given year. This could be verified with empirical evidence gathered through field measurement campaigns or through coupled atmosphere-ocean models. However, these are very scarce and typically extend over a single ice season. The logistics involved in data collection in the traits is immense. Straneo and Saucier (2008) provide an estimate of annual net volume transport into Foxe Basin through Fury and Hecla Strait of 0.07 (186 cm/y) based on April and May velocity measurements in 1962 and summer measurements in 1968. The estimated annual heat export through Hecla and Fury Strait with assumed winter and summer temperatures is estimated as -1.8 TW (-48 MJ/m2/y).

Ridenour et al. (2021) provide volume and heat transport estimates for Hudson Strait based on the only existing complete-year monitoring in Hudson Strait for the

2008/09 ice season. They estimate an August 2008 and September 2009 energy export through HS of -8.1 and -9.2 TW (approximately -214 and -243 MJ/m^2/y). These were years when annual Qs from ERA5 was -136 and -21 MJ/m^2/y, respectively. While the 2008 fluxes are of the same order of magnitude, it should be noted that ice covered flows are typically much smaller and the year-long measured fluxes would also typically be much smaller.

Straneo and Saucier (2008) provide annual estimates of heat transport through Hudson Strait based on moorings from August 2004 to August 2005 with supplemental estimates of temperatures. Their estimates for annual net outflow are between -2.2 and -3.9 TW or -58 and -103MJ/m2/y, respectively. The corresponding ERA5 estimates are -35 and 41 MJ/m2/y for the two calendar years. Both estimates assume steady state conditions. Interpretating these comparisons are limited in all cases because first, all the field-based estimates are taken from moorings across the mid-point of HS, and none consider the surface energy exchange with the atmosphere from HS itself. From this analysis for Hudson Strait ERA5 indicates a persistent negative energy budget averaging -78.1 MJ/m^2/y over the study period. Second, because this analysis is based on calendar years it is often inconsistent with field campaigns which span two open water seasons.

Subsurface heat surpluses (Qs) underwent a northward redistribution over the study period, shifting from localized anomalies in James Bay and southern Hudson Bay during the 1980s to basin-wide warming extending into Hudson Strait by the 2020s. Fourth, ice phenology changed markedly: the ice-covered season has shortened while the open-water season lengthened by several weeks across all sub-basins, with Hudson Strait experiencing the steepest declines in sea-ice cover, Tivy et al, (2011) and Hochheim and

Barber (2014) found it was at a rate of about ~4% per decade. The energy budget revealed a delicate balance between increased radiative gains and convective losses, though long-term reductions in latent and sensible heat fluxes suggest a possible trend toward energy retention., meaning there is more energy remaining in the overall system over time. The role of sensible heat transfer from precipitation is miniscule.

The large contrast between Foxe Basin and James Bay in terms of ice-cover and almost every aspect of the energy budget coincides with their latitude. But the early decades show Foxe Basin also being exceptionally windy which seems to have more recently dissipated. This is possibly due to changes in timing and positioning of the polar front in the summer season. The linear trends in Q_S are less significant and explain less of the inter-annual variability than the non-linear patterns which exist in the vertical temperature gradient, both convective fluxes and the interannual variability in surface temperatures. Finally, while ERA5 captured long-term patterns effectively, model biases and coarse parameterizations limited representation of critical fine-scale processes (Crawford et al., 2023, 2024). Collectively, these findings demonstrate that the HBC is transitioning from a seasonally ice-dominated marginal sea to a system increasingly characterized by persistent open-water conditions, with profound implications for ecosystems, Indigenous livelihoods, and climate feedbacks.

5.2 Energetics and the Ice–Albedo Feedback

The most robust finding of this thesis is the intensification of the ice–albedo feedback across the HBC. All sub-basins exhibited significant increases in net shortwave radiation (K*), despite no detectable increase in incoming solar flux. This confirms that changes in surface reflectivity, not atmospheric inputs, are driving the trends in the regional energy imbalance (Hochheim & Barber, 2010). As snow and sea ice retreat, albedo decreases from ~0.85 in winter to values as low as 0.40 over melt ponds and open water, substantially increasing absorbed solar energy (Bello & Higuchi, 2019). This process produces nonlinear effects. Once ice extent decreases below a threshold, absorption accelerates further melt and delays subsequent freeze-up, amplifying seasonal transitions (Tivy et al., 2011). These results mirror pan-Arctic observations of earlier breakup and later freeze-up but these show an amplified regional signal in the HBC, where shallow bathymetry, restricted oceanic circulation, and strong freshwater input limit vertical mixing and enhance surface warming (Saucier et al., 2004). Interannual variability remains high, influenced by synoptic-scale processes such as the Arctic Oscillation (AO) and North Atlantic Oscillation (NAO), which alter wind fields and temperature gradients (Deser et al., 2000; Bello & Higuchi, 2019). Nevertheless, the long-term signal is clear: radiative gains are outpacing losses, and this imbalance is accelerating the shift toward longer open-water seasons and reduced ice persistence. These findings reinforce the need to examine seasonal variations in the surface energy budget to evaluate whether the ERA5 model is internally consistent in both generating ice and melting ice in a cryogenic year (Crawford et al., 2023).

5.3 Spatial Redistribution of Subsurface Heat Flux

A second key outcome is the basin-wide redistribution of subsurface heat fluxes (Qs). In the early 1980s, net heat gains were largely confined to shallow southern sub-basins, such as James Bay and southwestern Hudson Bay. By 2024, warming anomalies extended across central Hudson Bay and into Hudson Strait, indicating that subsurface heat exchange is no longer a localized phenomenon but a basin-wide process (Kuzyk, 2014). This progression reflects multiple drivers. Freshwater inflows from major rivers such as the Nelson, Churchill, and La Grande enhance stratification, reducing vertical mixing and limiting heat loss to the atmosphere (Déry et al., 2011). At the same time, Hudson Strait functions as an energetic corridor, facilitating exchange with the Labrador Sea (Saucier et al., 2004). Oscillating Qs in the Strait suggests that redistribution is influencing not only internal basin energetics but also external ocean–atmosphere interactions. Persistent subsurface warming also creates thermal memory. Stored heat prolongs open-water periods, delays freeze-up and preconditions the system for earlier breakup in subsequent years (Hochheim & Barber, 2014). This helps explain why the HBC exhibits accelerated ice loss compared to deeper Arctic basins: its shallow structure increases susceptibility to hysteresis effects. A possible explanation is that the flash freezing events that can be observed throughout the waterbodies during the FU season and subsequently the increasingly lengthy BU season observances.

Five sample years were chosen from the 45-year study period for spatial analysis due to either their being beginning or end points (1980 and 2024), being the most neutral overall (1987 and 2005), or for being the year which showed the most overall energy loss (2011). Beginning with the first year of the study period, 1980 (Fig 24a), there are a couple hotspots we can observe at the mouths of the Nelson River, and Ungava Bay, this year exhibited an annual range of Q_S spanning from -1193 MJ/m^2/y to 1533 MJ/m^2/y (total range of 2716 MJ/m^2/y). The area of the bay which experienced the largest gains was at the base of JB, whereas the area which experiences the largest losses in energy was on the west coast of HB near the border of Manitoba and Nunavut; the spatial distribution pattern of Q_S

for this annuum gradually decreased from JB, where there was a substantial gain in energy over the year, to the western coast of HB as mentioned above. The most northern region of the study site, FB, observed a range of energy loss of -700 $MJ/m^2/y$ to around 0 $MJ/m^2/y$.

The two near-neutral years, 1987 and 2005 (Fig 24b, c) exhibit the same relative patterns. They have hotspots (annual energy surpluses) at the mouth of the Nelson River and a slightly less prominent one in Ungava Bay compared to the year 1980. The largest cold spots (annual energy deficits) were seen off the west coast of FB and the northernmost section of HS. The overall spatial pattern for both years is also like that of 1980 where the annual losses in Q_S increase from JB up to FB. 1987 (Fig 24b) has an overall range in energy consumption/loss of 2594 $MJ/m^2/y$, with the minimum of -941 $MJ/m^2/y$ and the maximum of 1653 $MJ/m^2/y$. Whereas 2005 (Fig 24c) has the largest range in energy from -1099 $MJ/m^2/y$ to 1622 $MJ/m^2/y$ for a total observed range of 2721 $MJ/m^2/y$ over the entire HBC.

2011 (Fig 24d) was chosen to evaluate due to this year having the most negative mean Q_S (-312 $MJ/m^2/y$). There are no specific hotspots that can be pointed out for this year and there is an interesting pattern of substantial energy loss on both the east and west coasts of the HB extending into the entire region of HS. There is also an odd pattern occurring in the middle of the HB with seemingly random spots of energy gain compared to the surrounding area. For 2011, the maximum of 619 $MJ/m^2/y$, and the minimum of -1552 $MJ/m^2/y$ (range of 2171 $MJ/m^2/y$).

The final year of interest for spatial distribution patterns was the final year of study, 2024 (Fig 24e). While this year, at first glance, may seem to be experiencing the largest amount of loss compared to the other years, the range of energy gained/lost over the year was actually the smallest with a minimum of -854 MJ/m^2/y, and a maximum of 1096 MJ/m^2/y for a range of 1950 MJ/m^2/y. 2024 did experience a “hot zone” which spanned from the base of JB to the middle of HB. Those regions are also where the most surplus energy gained was observed, however, there is also an observed latitudinal gradient from mid HB up to the northern tip of FB.

In general, the annual minima seem to control the mean (Qs_{HBC} = 0.79 Qs_{min}+ 895, R^2=0.88, p<0.01) whereas there are no significant relationships between Qs_{HBC} and the maxima or range in Qs. A portion of an annual surplus will go into warming or ice melt locally but generally the patterns are a consequence of advection. Zones which exhibit an annual surplus must export surface energy to maintain a zero balance, which may result from the net export of warmer water or net import of ice. Conversely, zones with an annual deficit must import energy to maintain an annual zero balance, either by importing warmer water or exporting ice. The coastal zones tend to exhibit the most severe annual deficits particularly along the west coast of HB and FB. Hudson Strait exhibits the most anomalous patterns as the annual Qs shifts from surplus through neutral to deficit.

5.4 Model Performance and Biases

While ERA5 offered valuable temporal and spatial coverage, limitations in model performance must be acknowledged. ERA5 prescribes sea surface temperatures and sea-ice concentrations rather than generating them dynamically, limiting representation of two-way feedbacks. This is particularly problematic in marginal seas like the HBC, where snow–ice formation, melt pond evolution, and riverine freshwater contributions play major roles in thermodynamics but remain underrepresented (Hochheim & Barber, 2010).

Nevertheless, ERA5 captured many observed trends with strong significance, including warming air and surface temperatures, radiative forcing increases, and sea-ice phenology shifts. Its strengths lie in the integration of observational datasets and consistency across decades, making it a reliable tool for long-term analysis. However, advancing toward coupled Earth system reanalyses remains critical for capturing the unique dynamics of the HBC (Crawford et al., 2023).

5.5 Ecological and Societal Implications

5.5.1 Primary Production and the Marine Food Web

Sea-ice loss in the HBC is restructuring primary production and the marine food web. Earlier breakup alters the timing of under-ice phytoplankton blooms, which are essential for zooplankton grazers (Steiner et al., 2015). Mismatches between bloom onset and grazing cycles may disrupt energy transfer to higher trophic levels, affecting fish populations and marine mammals.

Extended open-water periods also enhance wind-driven mixing, which in some regions may increase nutrient availability but in others exacerbate stratification due to freshwater inflows (Saucier et al., 2004). The ecological outcome is thus spatially heterogeneous, with potential for localized productivity increases but basin-wide instability in trophic interactions (Barbedo et al., 2020).

5.5.2 Polar Bears and Marine Mammals

Polar bears in Hudson Bay rely on seasonal ice to access seals, and population declines of approximately 50% over the past four decades highlight the severity of habitat loss (Dickie, 2024). Earlier breakup shortens the hunting season, while delayed freeze-up prolongs fasting periods, with negative impacts on reproduction and survival (Hochheim & Barber, 2014). Marine mammals such as beluga whales and ringed seals are also vulnerable. Belugas depend on predictable ice-edge habitats for feeding and migration, while seals require stable ice for pupping. Shifts in ice timing and thickness directly disrupt these life-history events, with cascading consequences for food web stability (Soriot et al., 2025).

5.5.3 Indigenous Communities

For Inuit and Cree communities, changing ice regimes threaten cultural continuity, food security, and safety. Ice routes historically used for hunting and travel are increasingly unpredictable, raising risks for on-ice travel (Gearheard et al., 2010). Extended open-water seasons also shift species distributions, making access to traditional food sources more difficult. These results underscore the need to integrate Indigenous knowledge into monitoring and adaptation strategies. Local expertise provides fine-scale insights into ice conditions and ecological changes, complementing reanalysis data and enhancing resilience (Gearheard et al., 2010).

5.6 Research Gaps and Future Directions

Several research gaps emerge from this analysis. First, lateral fluxes—including river discharge, tidal mixing, and Hudson Strait exchange—are poorly constrained yet play critical roles in modulating subsurface heat storage (Saucier et al., 2004; Déry et al., 2011). Future work should quantify these fluxes to better understand basin-scale energetics. Second, vertical coupling processes such as snow–ice conversion, melt pond evolution, and light penetration are underrepresented in ERA5 yet central to albedo dynamics. High-resolution regional models should prioritize these processes. Third, improved downscaling of global models is urgently needed. The biases identified in CMIP6 outputs demonstrate that pan-Arctic models are insufficient for marginal seas. Regional models calibrated with observational and Indigenous data will be essential for reliable forecasting (Crawford et al., 2023, 2024). Finally, greater integration and evaluation of lateral energy transfers and salinity are recommended for future areas of research. Understanding how/if any changes in salinity impact changes in flows into/out of the system, or vertical mixing are critical to the next phases of research into the energetics of the Hudson Bay Complex. Continued investigations into these aspects would only enhance what knowledge we think we have on energy systems and thermodynamics, and an improved understanding could only lead to increased areas of research and once again, more knowledge production regarding these complex systems.

The Hudson Bay Complex is undergoing a rapid and systemic thermodynamic transformation characterized by intensified radiative forcing, redistribution of subsurface heat, and shifts in seasonal sea-ice cover. These changes are not solely the result of atmospheric warming but arise from interacting feedbacks within the ocean–ice–atmosphere system. The consequences extend across scales, from disrupted phytoplankton bloom timing and declining polar bear populations to cultural and food security challenges for Indigenous communities. By conducting a basin-wide audit of energetics, this study provides new insights into the mechanisms driving one of the most climatically sensitive marine regions in the Northern Hemisphere. The findings emphasize the urgency of advancing coupled modeling frameworks, expanding ecological monitoring, and integrating

Indigenous knowledge. The trajectory of the HBC over the next half-century will depend not only on global emission pathways but also on the capacity of science and policy to respond to these intertwined ecological and societal challenges.

Chapter 6 - Conclusion

This thesis has examined the thermodynamic evolution of the Hudson Bay Complex (HBC) from 1980 to 2024, drawing on ERA5 reanalysis data to interpret changes in the surface energy budget, subsurface heat fluxes, and sea-ice seasonality. The findings reveal several interrelated processes that collectively demonstrate the HBC is undergoing a profound climate-driven transformation. First, linear increases in net shortwave (K*) and incoming longwave radiation (L↓) confirm that surface-state changes, particularly declining albedo, are amplifying warming across all subregions. The ice–albedo feedback, long theorized as a major driver of Arctic change, is now clearly manifested in the HBC, reinforcing longer open-water seasons and shorter ice-covered periods. Second, mean annual surface temperatures and air temperatures have been increasing significantly over the past 45 years. Minimum surface temperatures have been increasing faster than maximum surface temperatures.

Third, superimposed on the linear changes in radiative forcing and temperature are highly significant non-linear convective losses of surface energy to the atmosphere. These are primarily in response to nonlinear patterns in the vertical temperature gradient over time. Fourth, the combined impact of radiative gains and convective losses results in a long-term surface energy surplus, annually. But notably, the Hudson Bay Complex undergoes large, and sometimes abrupt, annual swings from an energy surplus to an energy deficit over the study period. These must be accommodated by internal energy gains leading to an increase in temperature or decrease in ice amount and/or by marine advection out through Hudson Strait. A lack of empirical evidence limits the ability to definitively partition the annual surpluses and deficits into the two possible outcomes. Notably, while large energy surpluses have occurred in the most recent two years studied, comparable surpluses occurred during seven previous years extending back to 1981.

Fifth, while freshwater river discharge into the HBC has long been considered a major factor responsible for annual net flow volumes exiting through Hudson Strait, there is also an annual excess of precipitation over evaporation increasing the annual freshwater inputs to the HBC by approximately 50% over those due to discharge alone. Sixth, the redistribution of subsurface heat fluxes (Qs) from localized southern zones in the early 1980s to widespread coverage of central Hudson Bay by 2024 underscores that surplus energy is no longer confined to marginal seas but is spreading basin-wide. This pattern is consistent with earlier observations of shifting ice regimes (Hochheim & Barber, 2014; Bello & Higuchi, 2019) and signals a systemic reorganization of the HBC's energy balance.

The ecological and societal implications of these physical changes are substantial. Altered bloom dynamics threaten food-web stability, polar bear populations are in decline, and Indigenous communities face increased risks and disruptions to cultural continuity. These cascading consequences highlight that the HBC's thermodynamic transition is not only a scientific concern but also a pressing ecological and human one.

At the same time, we have identified several research gaps and limitations. The coarse resolution of ERA5 smooths fine-scale processes such as polynyas and river plumes, while lateral and vertical fluxes remain underrepresented. Ecological datasets and Indigenous knowledge have not yet been fully integrated into physical assessments, representing a critical frontier for future research. Its rapid transformation underscores the urgency of improved coupled modeling, continued monitoring, and interdisciplinary approaches. These findings provide essential context for the concluding chapter, which synthesizes the major contributions of this thesis, evaluates its significance, and outlines directions for future work.

This thesis has demonstrated that the Hudson Bay Complex is undergoing a rapid thermodynamic transformation driven by enhanced radiative forcing and feedback loops. Net radiation has increased across all subregions, subsurface heat fluxes have intensified and expanded northward, and sea-ice duration has declined. Together, these results indicate a fundamental reorganization of the HBC's seasonal energy balance. These findings align with and extend previous work by Hochheim & Barber (2014), Bello & Higuchi (2019), and Crawford et al. (2023), reinforcing the conclusion that the HBC is one of the most climate-sensitive marine systems in the Arctic. The ecological and societal implications are profound, from altered primary production to polar bear declines and increased challenges for Indigenous communities.

By conducting a basin-wide audit of energetics, this thesis moves beyond descriptive accounts of ice loss to provide mechanistic insights into the processes driving change. It emphasizes that air temperature alone cannot explain HBC dynamics—rather, the system is shaped by complex, interacting feedback that must be incorporated into both science and policy responses.

Now that the Port of Churchill is being considered as a major marine transit post for Trans-Atlantic Shipping, research like this is more important than ever. The transportation of critical materials such as potash, grain, liquefied natural gas (LNG) and even oil from

Canada to Europe would be a major political and economic benefit to both countries. For these transportation routes from the Atlantic through Hudson Strait and into the main Basin of Hudson Bay to be useful, their open-water and ice-covered seasons need to be understood, unpredictability is detrimental for this initiative. By understanding the patterns of sea-ice persistence, people and the regional biota will benefit greatly. The local populations of Beluga whales and Polar Bears are at risk when their regular seasons shift; these unpredictability's and changes have a direct effect on the food storage and availability, habitat regularity, and reproduction seasons for these essential beings. This thesis brought forth more understanding of how the seasons are changing and the energetic units responsible for those changes being observed.

References

Andrews, J., Babb, D., & Barber, D. G. (2018). Climate change and sea ice: Shipping in Hudson Bay, Hudson Strait, and Foxe Basin (1980–2016). Elementa: Science of the Anthropocene, 6, 19. https://doi.org/10.1525/elementa.281

Barbedo, L., Bélanger, S., & Tremblay, J.-É. (2020). Climate control of sea-ice edge phytoplankton blooms in the Hudson Bay system. Elementa: Science of the Anthropocene, 8(1), 039. https://doi.org/10.1525/elementa.039

Bello, R., & Higuchi, K. (2019). Changing surface radiation and energy budgets of the hudson bay complex using the north american regional reanalysis (Narr) model. Arctic Science, 5(4), 218–239. https://doi.org/10.1139/as-2018-0034

Catchpole, A. j. w., & Halpin, J. (1987). Measuring Summer Sea Ice Severity in Eastern Hudson Bay 1751–1870. Canadian Geographies / Géographies Canadiennes, 31(3), 233–244. https://doi.org/10.1111/j.1541-0064.1987.tb01237.x

Crawford, A. D., Rosenblum, E., Lukovich, J. V., & Stroeve, J. C. (2023). Sources of seasonal sea-ice bias for CMIP6 models in the Hudson Bay Complex. Annals of Glaciology, 64(92), 236–253. https://doi.org/10.1017/aog.2023.42

Derksen, C., Smith, S. L., Sharp, M., Brown, L., Howell, S., Copland, L., Mueller, D. R., Gauthier, Y., Fletcher, C. G., Tivy, A., Bernier, M., Bourgeois, J., Brown, R., Burn, C. R., Duguay, C., Kushner, P., Langlois, A., Lewkowicz, A. G., Royer, A., & Walker, A. (2012). Variability and change in the Canadian cryosphere. Climatic Change, 115(1), 59–88. https://doi.org/10.1007/s10584-012-0470-0

Deser, C., Walsh, J. E., & Timlin, M. S. (2000). Arctic Sea Ice Variability in the Context of Recent Atmospheric Circulation Trends. https://journals.ametsoc.org/view/journals/clim/13/3/1520-0442_2000_013_0617_asivit_2.0.co_2.xml

Dickie, G., & Dickie, G. (2024, June 13). Record low May sea ice rings alarm bells for Canada's Hudson Bay polar bears. Reuters.

https://www.reuters.com/business/environment/record-low-may-sea-ice-rings-alarm-bells-canadas-hudson-bay-polar-bears-2024-06-13/

Gearheard, S., Pocernich, M., Stewart, R., Sanguya, J., & Huntington, H. P. (2010). Linking Inuit knowledge and meteorological station observations to understand changing wind patterns at Clyde River, Nunavut. Climatic Change, 100(2), 267–294. https://doi.org/10.1007/s10584-009-9587-1

Gough, W. A., Cornwell, A. R., & Tsuji, L. J. S. (2004). Trends in Seasonal Sea Ice Duration in Southwestern Hudson Bay. ARCTIC, 57(3), 299–305. https://doi.org/10.14430/arctic507

Hochheim, K. P., & Barber, D. G. (2010). Atmospheric forcing of sea ice in Hudson Bay during the fall period, 1980–2005. Journal of Geophysical Research: Oceans, 115(C5). https://doi.org/10.1029/2009JC005334

Hochheim, K. P., & Barber, D. G. (2014). An Update on the Ice Climatology of the Hudson Bay System. Arctic, Antarctic, and Alpine Research, 46(1), 66–83. https://doi.org/10.1657/1938-4246-46.1.66

Kirillov, S., Babb, D., Dmitrenko, I., Landy, J., Lukovich, J., Ehn, J., Sydor, K., Barber, D., & Stroeve, J. (2020). Atmospheric Forcing Drives the Winter Sea Ice Thickness Asymmetry of Hudson Bay. Journal of Geophysical Research: Oceans, 125(2), e2019JC015756. https://doi.org/10.1029/2019JC015756

Munir, R. (2020.). Changes in The Seasonality of Sea Ice and The Underlying Mechanisms Across Hudson Bay (HB) From 1979-2018. MSc Thesis, Graduate Program in Geography, Faculty of Environmental and Urban Change, York University, xx pp.

Ridenour, N. A., Straneo, F., Holte, J., Gratton, Y., Myers, P. G., & Barber, D. G. (2021). Hudson Strait inflow: Structure and variability. Journal of Geophysical Research: Oceans, 126, e2020JC017089. https://doi.org/10.1029/2020JC017089

Saucier, F. J., & Dionne, J. (1998). A 3-D coupled ice-ocean model applied to Hudson Bay, Canada: The seasonal cycle and time-dependent climate response to atmospheric forcing and runoff. Journal of Geophysical Research: Oceans, 103(C12), 27689–27705. https://doi.org/10.1029/98JC02066

Saucier, F. J. S., Senneville, S., Prinsenberg, S., Roy, F., Smith, G., Gachon, P., Caya, D., & Laprise, R. (2004). Modelling the sea ice-ocean seasonal cycle in Hudson Bay, Foxe Basin and Hudson Strait, Canada. Climate Dynamics, 23, 303–326. https://doi.org/10.1007/s00382-004-0445-6

Soriot, C., Stroeve, J., & Crawford, A. (2025). Record Early Sea Ice Loss in Southeastern Hudson Bay in Spring 2024. Geophysical Research Letters, 52(4), e2024GL112584. https://doi.org/10.1029/2024GL112584

Steiner, N., Azetsu-Scott, K., Hamilton, J., Hedges, K., Hu, X., Janjua, M. Y., Lavoie, D., Loder, J., Melling, H., Merzouk, A., Perrie, W., Peterson, I., Scarratt, M., Sou, T., & Tallmann, R. (2015). Observed trends and climate projections affecting marine ecosystems in the Canadian Arctic. Environmental Reviews, 23(2), 191–239. https://doi.org/10.1139/er-2014-0066

Straneo, F., & Saucier, F. J. (2008). The Arctic–Subarctic Exchange Through Hudson Strait. In R. R. Dickson, J. Meincke, & P. Rhines (Eds.), *Arctic–Subarctic Ocean Fluxes: Defining the Role of the Northern Seas in Climate* (pp. 249–261). Springer Netherlands. https://doi.org/10.1007/978-1-4020-6774-7_11

Stroeve, J. C., Serreze, M. C., Holland, M. M., Kay, J. E., Malanik, J., & Barrett, A. P. (2012). The Arctic's rapidly shrinking sea ice cover: A research synthesis. Climatic Change, 110(3), 1005–1027. https://doi.org/10.1007/s10584-011-0101-1

Tivy, A., Howell, S. E. L., Alt, B., McCourt, S., Chagnon, R., Crocker, G., Carrieres, T., & Yackel, J. J. (2011). Trends and variability in summer sea ice cover in the Canadian Arctic based on the Canadian Ice Service Digital Archive, 1960–2008 and 1968–2008. Journal of Geophysical Research: Oceans, 116(C3). https://doi.org/10.1029/2009JC005855

Appendix A

Mean 45 Year Energy Budget (MJ/m²/y) & Water Budget [mm]					
	FB	HB	HS	JB	HBC
Kex	6535	7518	7189	8446	7373
$K\downarrow$	3582	4062	3726	4626	3972
K^*	1719	2249	2216	2668	2188
$L\downarrow$	7345	7873	7822	8270	7808
L^*	-1297	-1282	-1318	-1243	-1287
Q^*	423	967	898	1424	900
$K^* + L\downarrow$	9064	10123	10038	10938	9995
Q_H	-242	-343	-453	-197	-336
Q_E	-253	-484	-423	-466	-439
Q_P	0.8	-0.1	0.6	2.2	0.2
Q_{Lf}	-73	-77	-100	-80	-80
Q_S	-147	55	-82	677	40
T_0 [°C]	-10.2	-6.3	-6.2	-3.6	-6.9
T_2 [°C]	-10.4	-6.8	-6.9	-3.6	-7.4
T_0 - T_2 [°C]	0.28	0.51	0.66	0.02	0.47
Max T_0 [°C]	12.1	15.2	9.4	15.9	13.0
Min T_0 [°C]	-43.7	-40.3	-37.0	-33.3	-38.6
P	376	502	561	692	502
SF	226	232	305	248	242
RF	150	270	256	444	260
E	101	194	169	188	176
P-E	275	309	392	504	327
SIC (%)	64	51	45	47	52
Albedo (%)	52	45	40	42	45
Bowen Ratio	0.96	0.71	1.07	0.42	0.77
Days >90% IC (#)	179	152	100	129	147
Days >90% OW (#)	90	147	150	159	139